

---

# MOLECULAR GAS CONTENT IN DUST-RICH VIRGO GALAXIES. I. FIRST RESULTS FROM PMO TELESCOPE OBSERVATIONS

---

A PREPRINT

**ZhiYong Hu**

School of Physics and Electronic Information Engineering, Qinghai Normal University, Xining 810000, China

**JingFu Hu**

School of Physics and Electronic Information Engineering, Qinghai Normal University, Xining 810000, China

**YiPing Ao**

Purple Mountain Observatory

Chinese Academy of sciences, 10 Yuanhua Road, Nanjing, Jiangsu 210023, People's Republic of china

School of Astronomy and Space Sciences

University of cience and Technology of China, Hefei, Anhui 230026, People's Republic of china

March 11, 2025

## ABSTRACT

In this study, we used the 13.7m telescope at Qinghai Station to observe CO data in 48 galaxies in Virgo clusters, of which 41 sources observed CO signals. The properties of molecular gas are deduced by co-to- $H_2$  factor. We also collected and investigated the relationship between  $M_{H_2}$  and other galactic properties ( $M_B$ ,  $L_K$ , sfr, and  $def_{HI}$ ). We found correlations between  $M_{H_2}$  and  $M_B$ ,  $L_K$ , sfr, and  $def_{HI}$ . It has the strongest correlation with  $L_K$ . There is a certain correlation between MB and MB, but the scattering is larger. For sfr, the more abundant the atomic and molecular gases, the stronger the sfr activity.

**Keywords** galaxies: clusters: individual(Virgo) - galaxies:star formation rate - molecular data(CO,  $H_2$ )

## 1 Introduction

In galaxy clusters, the distribution of molecular gas is influenced by the hot gas within the cluster. Galaxies in clusters can lose gas due to interactions with hot gas. In addition, galactic interactions in galaxy clusters also affect the distribution of molecular gas and star formation (Braine & Combes 1993; Combes et al. 1994; Casasola et al. 2004). (Kenney & Young, 1989; Boselli et al. 1997). The distribution of molecular gas in the interior of a galaxy is usually closely related to star formation activity. The dissipation time scale of molecular gas (that is, the time it takes for molecular gas to transform into stars) varies from galaxy to galaxy, but is generally related to the star formation rate (SFR) of the galaxy.

The proximity of the Virgo Cluster makes it possible to observe its member galaxies with excellent spatial resolution. The Virgo cluster has been the object of recent multi-band observations, for example HI (Chung et al. 2009), radio (Yun, Reddy, & Condon. 2001), IR (Spitzer (Kenney et al. 2012)), FIR (Planck Collaboration. 2014 & Herschel Virgo Cluster Survey (HeViCS) (Edvige Corbelli & Simone Bianchi et al. 2012)), submm (Angus Mok et al. 2016 use JCMT), optical (Côté et al. 2004 HST/ACS Virgo Cluster Survey & Suk Kim & Soo-Chang Rey. et al. 2014 SDSS),  $H\alpha$  (Koopmann et al. 2001), and UV (Brosch et al. 1997 and Voyer et al. 2014 use GALEX). Therefore, it is possible to complete the analysis and processing of the first batch of spectral line data of the member galaxies of the Virgo cluster through the joint analysis of a large number of multi-band data and the CO data currently observed by us, and combine the multi-band data to study the evolution process of galactic gas in the cluster environment and its relationship with the star formation process.

The section 2 introduces sample selection and observation. The section 3 introduces the collection of multi-band data. The section 4 describes the data processing methods. In section 5 we analyze our results and discussion. Section 6 summarizes the main conclusions of this work.

## 2 Sample selection and observations

### 2.1 Sample selection

The sample observed at the 13.7m telescope is defined by the following criteria: i) Selected from the extend virgo clusters catalog (EVCC) directory (Suk Kim & Soo-Chang Rey. et al. 2014), ii) The flux of 857Ghz via the PLanck (Planck Collaboration. 2014) satellite is selected from high to low of Sources for which no proceed co observations have been made in the EVCC ( because Far-infrared radiation is closely related to that of interstellar dust. Dust particles absorb shorter wavelengths of light and re-radiate longer wavelengths of infrared light, including the far infrared band. This helps us understand the properties of the interstellar medium, including the distribution and dynamics of gas and dust, Therefore, it can be considered that the higher the flow rate of the fir band, the higher the probability of observing CO). The basic information of these sources is given in Table 1, such as: name, ra, dec, v, distance.

Table 1: EVCC Ra Dec Type T

EVCC	RA h:m:s	DEC d:m:s	Type	T	Dist Mpc
EVCC429	12:21:55	+04:28:26.04	Sbc	4.00	24.2
EVCC2159	12:32:45	+00:06:50.04	Scd	6.00	8.3
EVCC2184	12:36:50	+13:09:55.08	Sab	2.40	16.7
EVCC1099	12:43:33	+11:34:51.24	SABc	5.10	16.7
EVCC171	12:12:46	+10:51:55.8	Scd	6.90	16.7
EVCC2174	12:35:27	+14:29:43.8	Sb	3.10	15.0
EVCC233	12:15:39	+13:54:07.92	Sc	4.90	16.7
EVCC808	12:31:39	+03:56:23.64	Scd	7.40	14.5
EVCC1314	13:11:37	+22:54:55.44	Sc	5.10	42.5
EVCC2209	12:42:32	-00:04:50.52	Sc	5.00	14.4
EVCC952	12:36:56	+14:13:04.08	Scd	6.40	16.7
EVCC84	12:02:42	+01:58:37.56	Sa	1.30	33.7
EVCC884	12:34:03	+07:41:57.48	S0	-1.90	17.3
EVCC1281	13:00:39	+02:30:04.68	Sc	5.10	16.8
EVCC1074	12:42:41	+14:17:44.16	Sbc	5.80	16.7
EVCC107	12:08:11	+02:52:42.96	Sc	5.00	22.9
EVCC1202	12:51:55	+12:04:58.8	Sb	3.20	33.7
EVCC1182	12:49:39	+15:09:56.52	S0-a	-0.90	16.7
EVCC673	12:27:45	+13:00:39.6	Sa	0.60	16.7
EVCC59	11:55:57	+06:44:55.32	Sb	3.20	36.8
EVCC104	12:07:37	+02:41:28.32	SBcd	7.30	22.8
EVCC574	12:25:42	+07:13:05.16	SBc	6.00	22.9
EVCC631	12:26:55	-00:52:39.36	SABa	1.10	
EVCC461	12:22:42	+09:19:57.72	Sc	5.50	22.9
EVCC497	12:23:54	-03:26:34.8	Sbc	3.90	
EVCC153	12:11:53	+24:07:23.88	Sbc	4.00	43.9
EVCC488	12:23:39	+06:57:15.12	Sb	3.00	22.9
EVCC439	12:22:06	+09:02:37.32	SBb	3.20	16.4
EVCC1080	12:42:52	+13:15:25.56	Sbc	3.60	21.0
EVCC126	12:10:38	+16:01:59.16	SABc	4.90	16.7
EVCC1178	12:49:12	+03:23:19.68	Sc	5.90	16.6
EVCC1282	13:00:59	-00:01:39.72	Sc	5.80	17.8
EVCC1217	12:53:21	+01:16:09.12	Sc	6.00	20.2
EVCC996	12:39:19	-00:31:53.76	Sd	7.90	
EVCC587	12:25:58	+03:25:47.64	Sc	5.70	26.1
EVCC660	12:27:26	+06:15:50.04	Sb	3.50	16.4

EVCC	RA h:m:s	DEC d:m:s	Type	T	Dist Mpc
EVCC1223	12:53:51	+09:42:36.36	SBc	4.60	38.9
EVCC1069	12:42:31	+03:57:31.32	Ir	9.60	16.6
EVCC1104	12:43:51	-00:33:39.6	SABc	5.90	
EVCC635	12:26:58	+02:29:39.84	SBc	4.70	15.1
EVCC176	12:13:03	+07:02:20.04	SABa	2.00	24.2
EVCC208	12:14:39	+05:48:23.76	SABc	6.70	16.5
EVCC231	12:15:30	+09:35:06.36	Sd	7.70	16.7
EVCC1243	12:55:12	+00:06:57.96	SBcd	6.90	14.4
EVCC192	12:13:54	+13:10:21.72	SABb	4.10	30.1
EVCC776	12:30:27	+04:14:46.68	SABc	5.10	43.5
EVCC1209	12:52:44	+15:50:46.68	SBm	9.00	13.0
EVCC451	12:22:31	+15:32:16.44	Sab	2.10	16.7

## 2.2 13.7m telescope observations

### 2.2.1 13.7m telescope

The CO data used in this article was observed using the 13.7m telescope at the Qinghai station, The 13.7-m millimeter-wave radio telescope of Purple Mountain Observatory operates at 3200-m above the sea level near Delingha, Qinghai Province, China. Equipped with a superconducting SIS receiver, the telescope is used in the millimeter-wave band ranging from 85 to 115GHz. The superconducting imaging spectrometer has 3×3 beams, the single beam has a half-power beam width of 50" (115.2 GHz), the spacing distance between adjacent beams is 60 mm, and the corresponding spacing Angle is 175".

### 2.2.2 Method of observation

Starting from April 30, 2024, the observations will be made in an ON-OFF mode, with an integration time of 10 seconds each time, and a pointing calibration of the telescope will be performed before each observation. One source per day is observed for a total observation time of about 3 hours, and the observation time for each source is about 60 minutes. And our detection sensitivity can detect the molecular line emission of a significant number of dusty galaxies. The CO signal was observed in 46 galaxies, with an upper limit of  $3\sigma$  given for other sources.

## 2.3 Optical HI and FIR data

### 2.3.1 Optical data

The collected optical data are listed in Table 2 and will be compared with the CO data, The type of pattern shown in col(2) is: contains the machine-readable version of the Third Reference Catalogue of Bright Galaxies (RC2) by De Vaucouleurs et al. 1976, B-band in col(3) and BT-band in col(4), from De Vaucouleurs et al. 1976 (RC2 p33 rel.25) BT is the absolute magnitude.

Table 2: EVCC and optical data

EVCC	Bband mag	BT mag	Kband mag	$L_K$ $L_\odot$	cz km s <sup>-1</sup>	d25 KPC
EVCC429	10.16 ± 0.06	-21.76 ± 0.118	6.87 ± 0.09	8.31E+11	1613.5	28.30
EVCC2159	11.19 ± 0.08	-18.41 ± 0.133	7.38 ± 0.11	6.11E+10	1126.0	34.85
EVCC2184	10.18 ± 0.14	-20.93 ± 0.379	6.60 ± 0.08	5.07E+11	-235.0	40.55
EVCC1099	11.60 ± 0.48	-19.51 ± 0.572	8.07 ± 0.08	1.31E+11	1417.2	23.93
EVCC171	11.92 ± 0.07	-19.10 ± 0.211	9.64 ± 0.15	2.83E+10	441.9	35.96
EVCC2174	10.94 ± 0.06	-19.94 ± 0.073	7.18 ± 0.14	2.40E+11	486.0	32.36
EVCC233	11.78 ± 0.09	-19.33 ± 0.185	8.37 ± 0.01	9.94E+10	-156.8	16.96
EVCC808	12.11 ± 0.09	-18.70 ± 0.093	9.73 ± 0.25	2.14E+10	1746.4	17.58
EVCC1314	12.40 ± 0.07	-20.74 ± 0.159	8.78 ± 0.04	4.41E+11	2622.5	32.26

EVCC	Bband mag	BT mag	Kband mag	$L_K$ $L_\odot$	cz km s <sup>-1</sup>	d25 KPC
EVCC2209	12.27 ± 0.04	-18.52 ± 0.757	9.30 ± 0.07	3.14E+10	1721.0	15.45
EVCC952	11.92 ± 0.22	-19.19 ± 0.281	8.64 ± 0.15	7.75E+10	340.8	21.96
EVCC84	12.61 ± 0.10	-20.03 ± 0.307	10.77 ± 0.07	4.44E+10	1996.9	26.82
EVCC884	10.55 ± 0.09	-20.64 ± 0.094	6.48 ± 0.05	6.08E+11	427.3	35.07
EVCC1281	11.89 ± 0.09	-19.24 ± 1.046	8.68 ± 0.07	7.56E+10	959.7	20.26
EVCC1074	13.04 ± 0.07	-18.07 ± 0.144	9.27 ± 0.04	4.34E+10	232.6	19.84
EVCC107	11.96 ± 0.11	-19.84 ± 0.222	8.86 ± 0.14	1.19E+11	1287.1	22.67
EVCC1202	13.33 ± 0.02	-19.31 ± 0.24	9.51 ± 0.06	1.42E+11	1754.8	47.60
EVCC1182	11.60 ± 0.15	-19.51 ± 0.893	7.58 ± 0.05	2.06E+11	1190.6	31.03
EVCC673	10.97 ± 0.08	-20.14 ± 0.36	7.28 ± 0.06	2.71E+11	9.5	32.77
EVCC59	12.45 ± 0.03	-20.38 ± 0.235	8.98 ± 0.36	2.75E+11	2695.4	35.81
EVCC104	12.47 ± 0.08	-19.32 ± 0.33	10.39 ± 0.19	2.88E+10	1331.3	20.01
EVCC574	13.56 ± 0.07	-18.24 ± 0.239	9.79 ± 0.02	5.05E+10	1002.3	27.10
EVCC631	13.83 ± 0.03	-17.30 ± 0.501	10.17 ± 0.08	1.92E+10	2123.1	11.06
EVCC461	13.54 ± 0.06	-18.26 ± 0.26	9.26 ± 0.03	8.24E+10	1248.6	25.49
EVCC497	13.11 ± 0.07	-18.02 ± 0.248	8.96 ± 0.16	5.84E+10	2028.0	31.31
EVCC153	12.68 ± 0.19	-20.53 ± 0.496	9.38 ± 0.03	2.71E+11	2688.1	26.31
EVCC488	13.31 ± 0.38	-18.49 ± 0.503	9.00 ± 0.05	1.05E+11	1000.0	20.69
EVCC439	12.71 ± 0.06	-18.36 ± 0.366	8.73 ± 0.01	6.88E+10	983.4	28.79
EVCC1080	12.08 ± 0.10	-19.53 ± 0.100	8.81 ± 0.05	1.05E+11	1091.6	21.04
EVCC126	12.84 ± 0.19	-18.27 ± 0.331	9.65 ± 0.03	3.06E+10	2173.1	21.92
EVCC1178	12.79 ± 0.04	-18.31 ± 0.351	9.80 ± 0.07	2.63E+10	753.0	23.22
EVCC1282	12.59 ± 0.09	-18.66 ± 0.285	9.52 ± 0.05	3.92E+10	1188.6	14.65
EVCC1217	12.73 ± 0.07	-18.80 ± 0.343	9.01 ± 0.02	8.07E+10	1125.4	25.63
EVCC996	12.32 ± 0.04	-18.81 ± 0.328	10.21 ± 0.08	1.85E+10	1082.4	19.85
EVCC587	14.23 ± 0.12	-17.86 ± 0.541	10.17 ± 0.03	9.55E+10	1409.6	46.34
EVCC660	12.65 ± 0.09	-18.42 ± 0.510	9.56 ± 0.23	3.20E+10	1472.5	20.63
EVCC1223	13.07 ± 0.05	-19.88 ± 0.262	9.91 ± 0.07	1.31E+11	2860.9	28.62
EVCC1069	13.04 ± 0.06	-18.06 ± 0.272	9.95 ± 0.12	2.29E+10	732.4	12.72
EVCC1104	12.77 ± 0.09	-18.36 ± 0.415	10.11 ± 0.20	2.03E+10	2630.5	36.13
EVCC635	12.77 ± 0.06	-18.12 ± 0.532	9.67 ± 0.05	2.45E+10	1722.0	10.88
EVCC176	13.22 ± 0.04	-18.70 ± 0.287	9.12 ± 0.03	1.05E+11	2263.0	23.54
EVCC208	13.36 ± 0.05	-17.73 ± 0.198	10.25 ± 0.08	1.72E+10	2052.8	30.29
EVCC231	13.40 ± 0.05	-17.71 ± 0.330	9.46 ± 0.04	3.64E+10	637.9	11.09
EVCC1243	12.94 ± 0.10	-17.85 ± 0.334	11.59 ± 0.46	3.81E+09	1309.4	16.46
EVCC192	13.12 ± 0.06	-19.27 ± 0.110	9.35 ± 0.05	1.31E+11	2464.1	30.82
EVCC776	13.10 ± 0.03	-20.09 ± 0.255	9.77 ± 0.09	1.86E+11	2442.8	30.03
EVCC1209	13.41 ± 0.07	-17.16 ± 0.437	10.12 ± 0.22	1.20E+10	1306.2	15.14
EVCC451	12.48 ± 0.06	-18.63 ± 0.277	8.85 ± 0.11	6.39E+10	178.9	18.02

### 2.3.2 HI data

We use of H I sources extracted from the Arecibo Legacy Fast ALFA (ALFALFA) extragalactic survey (Riccardo Giovanelli, & Martha P. Haynes, et al. 2007, Brian R. Kent & Riccardo Giovanelli et al. 2008), initiated in 2005. Sources have been extracted from three-dimensional spectral data cubes exploiting a matched filtering technique and then examined interactively to yield global H I parameters. (Riccardo Giovanelli, & Martha P. Haynes, et al. 2007) The H I flux of the galaxy is given.

The H I mass is determined using the following relation:

$$M_{HI}(M_\odot) = 2.356 \times 10^5 d^2 S_{HI}$$

Where d is the distance to the source in MPC,  $S_{HI}$  is the flux of HI, in  $Jy km s^{-1}$ .

To measure the abundance of atomic gas in Virgo galaxies, we adopt the H I deficiency parameter as an indicator of atomic gas. The good correlation of H I mass and optical diameter in isolated galaxies allows a useful parameterization of the normalcy of any galaxy's H I content to be defined as (Giovanelli, R., & Haynes, M. P. 1983 GH83); In a study of the H I emission from 324 isolated galaxies, Haynes, M. P., & Giovanelli, R. 1984 (1984, hereafter HG84) demonstrated

that the H I mass of an isolated galaxy depends primarily on its optical diameter, and only slightly on its morphological type. Since the type dependence for Sa-Sm is slight, we follow GH83 in adopting an H I deficiency parameter which is independent of morphological type. The formula we use for the “expected” H I mass is (GH83):

$$\log M_{HI}(\text{isolated}) = 7.01 + 0.88 \log D_{H_0}^2$$

where  $M_{HI}$  is measured in solar units, and the optical diameter  $D_{H_0}$  is the Holmberg diameter, measured in kiloparsecs to a surface brightness of  $26.5 \text{ mag arcsec}^{-2}$ . The good correlation of H I mass and optical diameter in isolated galaxies allows a useful parameterization of the normalcy of any galaxy’s H I content to be defined as (GH83):

$$HI_{def} = \log M_{HI}(\text{isolated}) - \log M_{HI}(\text{actual})$$

### 2.3.3 FIR data

The FIR data used in this paper are two sky survey data, respectively Planck Catalog of Compact Sources (PCCS)(Planck Collaboration. 2014) 545 and 857 GHz flux in two band, And Herschel SPIRE(Edvige Corbelli & Simone Bianchi et al. 2012) Data 250,300,500  $\mu\text{m}$  flux in three bands. The Planck and Herschel data are listed in Table 2. These data will be compared with CO data.

The photutils<sup>1</sup> package in python is used to conduct photometry for Herschel, and the 2D Background and Noise Estimation is used to analyze the background noise. In order to shield the influence of sources on the background noise, It is considered that the pixel mask in the image is larger than the first median noise  $2\sigma$ , and the background noise of the image after the mask is analyzed once, and its root mean square is considered as the metering error.

## 3 Data reduction

### 3.1 CO data processing

The tool used in this article to process co data is GILDAS-CLASS(Pety 2005)<sup>2</sup>, GILDAS-CLASS is a software package for reducing spectroscopic data obtained on a single-dish telescope. It also has basic functionalities to reduce continuum drifts like pointing or focus.

First, find all the spectral lines where the observation file position error is 0, These lines are averaged and smoothed to  $V=4.1 \text{ km s}^{-1}$ , after which baseline fitting is performed, The rms noise level of the final spectra ranges between 7 mK and 13 mK in CO(1-0) (Table 3). Integrated intensities,  $I_{CO}$ , were calculated way is : we fitted a Gauss function (single-peak profiles) or a linear combination of the first two Hermite functions (double-peak profiles; Saintonge. 2007) to the spectra. We detected CO (1-0) emission lines in 42 of the first 48 galaxies, and gave an upper limit of  $3\sigma$  for undetected galaxies. In Figure 1, we give the spectral line intensity diagram after processing with class.

In Table 2 we list the following items:

1. rms: root mean square noise in mK for a velocity resolution of  $4.71 \text{ km s}^{-1}$ .
2.  $I_{CO}$ : velocity integrated CO line temperature  $T_{mb} dv$ , in  $\text{K km s}^{-1}$ , and its error;
3.  $V_{CO}$ : mean velocity of the CO line, in  $\text{km s}^{-1}$
4.  $W_{CO}$ : Velocity linewidth of CO spectrum, in  $\text{km s}^{-1}$

Conversion between main beam temperature in Kelvin and flux in Jansky ( $S_\nu$ ) for a point-like source were made using the relation

$$G = S_\nu / T_{mb} = 2k / (\pi r^2 / 4.0) \times 1.0 \times 10^{26} \times 0.51 / 0.38 [Jy / K]$$

Where  $k$  is the Boltzmann constant,  $r$  is the radius of the telescope 13.7m, and 0.51 and 0.38 are the main beam efficiency and lunar efficiency, respectively.

The CO luminosity is calculated as follows:

$$L_{CO} = 0.119 S_{CO} d^2$$

where  $d$  is the distance to the source in Mpc and  $S_{CO}$  is the total CO flux in  $\text{Jy km s}^{-1}$  (Kenney & Young, 1989). The molecular gas mass ( $M_{H_2}$ ) is calculated using a Galactic conversion factor of  $N(H_2)/I_{CO} = 2.8 \times 10^{20} \text{ cm}^{-2} (\text{K km s}^{-1})^{-1}$  (Bloemen et al(1986)) yielding:

<sup>1</sup><https://photutils.readthedocs.io/en/stable/index.html>

<sup>2</sup><https://www.iram.fr/IRAMFR/GILDAS/>

$$M_{H_2}[M_\odot] = 1.1 \times 10^4 D^2 S_{co}$$

where  $S_{CO}$  is the velocity integrated CO line intensity in  $\text{Jy km s}^{-1}$ ,  $D$  is the distance in Mpc.

Table 3: EVCC and CO data

EVCC	$V_{CO}$ $\text{km s}^{-1}$	$W_{CO}$ $\text{km s}^{-1}$	$T_{peak}$ K	$I_{CO}$ $\text{K km s}^{-1}$	$L_{CO}$ $L_\odot$
EVCC429	$1592.00 \pm 1.00$	$97.18 \pm 4.21$	0.170	$20.6 \pm 0.40$	3.61E+04
EVCC2159	$1126.20 \pm 2.60$	$94.52 \pm 6.75$	0.058	$5.90 \pm 0.30$	1.21E+03
EVCC2184	$-211.60 \pm 2.30$	$214.95 \pm 4.80$	0.112	$25.9 \pm 0.50$	2.16E+04
EVCC1099	$1426.10 \pm 2.80$	$93.46 \pm 5.09$	0.074	$7.30 \pm 0.40$	6.09E+03
EVCC171	$381.85 \pm 8.16$	$101.47 \pm 16.53$	0.022	$2.33 \pm 0.36$	1.78E+03
EVCC2174	$451.72 \pm 15.69$	$188.39 \pm 28.91$	0.014	$2.84 \pm 0.43$	1.91E+03
EVCC233	$-39.61 \pm 5.49$	$155.00 \pm 10.90$	0.040	$6.63 \pm 0.45$	5.53E+03
EVCC808	$1716.11 \pm 3.64$	$56.41 \pm 9.05$	0.035	$2.08 \pm 0.27$	1.31E+03
EVCC1314	$2727.01 \pm 6.72$	$113.37 \pm 12.18$	0.020	$2.44 \pm 0.27$	1.32E+04
EVCC2209	$1724.36 \pm 7.76$	$131.00 \pm 13.91$	0.021	$2.87 \pm 0.32$	1.78E+03
EVCC952	$322.25 \pm 3.93$	$84.79 \pm 8.09$	0.027	$2.43 \pm 0.21$	2.03E+03
EVCC84	$1971.71 \pm 6.78$	$261.07 \pm 13.59$	0.050	$13.96 \pm 0.70$	4.74E+04
EVCC884	$366.12 \pm 8.18$	$189.07 \pm 15.12$	0.042	$8.51 \pm 0.70$	7.61E+03
EVCC1281	$962.00 \pm 1.90$	$55.25 \pm 4.19$	0.079	$4.60 \pm 0.30$	3.88E+03
EVCC1074	$105.41 \pm 6.22$	$289.94 \pm 14.37$	0.043	$13.21 \pm 0.58$	1.10E+04
EVCC107	$1282.46 \pm 4.15$	$180.60 \pm 9.12$	0.059	$11.32 \pm 0.49$	1.77E+04
EVCC1202	$1841.64 \pm 10.51$	$293.06 \pm 25.49$	0.026	$8.06 \pm 0.59$	2.74E+04
EVCC1182	$1154.07 \pm 8.88$	$237.70 \pm 18.31$	0.035	$8.82 \pm 0.64$	7.35E+03
EVCC673	$219.98 \pm 6.87$	$95.01 \pm 14.61$	0.034	$3.45 \pm 0.46$	2.88E+03
EVCC59	$2639.91 \pm 10.53$	$191.95 \pm 21.68$	0.020	$4.12 \pm 0.44$	1.67E+04
EVCC104	$1292.76 \pm 3.74$	$33.65 \pm 6.53$	0.029	$1.05 \pm 0.21$	1.63E+03
EVCC574	$943.03 \pm 8.75$	$179.74 \pm 21.79$	0.024	$4.56 \pm 0.46$	7.15E+03
EVCC631	$2086.67 \pm 2.87$	$44.40 \pm 5.66$	0.037	$1.77 \pm 0.22$	1.49E+03
EVCC461	$1209.85 \pm 9.04$	$157.54 \pm 18.12$	0.020	$3.38 \pm 0.38$	5.30E+03
EVCC497	$2170.83 \pm 10.76$	$227.75 \pm 26.71$	0.023	$5.61 \pm 0.54$	4.73E+03
EVCC153	$2436.25 \pm 4.19$	$61.94 \pm 9.76$	0.035	$2.32 \pm 0.31$	1.34E+04
EVCC439	$1090.70 \pm 8.91$	$150.74 \pm 19.39$	0.015	$2.39 \pm 0.27$	1.92E+03
EVCC1080	$982.60 \pm 15.35$	$179.60 \pm 34.75$	0.008	$1.46 \pm 0.24$	1.92E+03
EVCC126	$2113.32 \pm 7.61$	$93.76 \pm 25.36$	0.017	$1.69 \pm 0.31$	1.41E+03
EVCC1178	$725.28 \pm 3.73$	$16.43 \pm 7.49$	0.195	$3.42 \pm 1.50$	2.82E+03
EVCC1282	$1238.42 \pm 6.13$	$40.19 \pm 10.29$	0.020	$0.87 \pm 0.23$	8.24E+02
EVCC1217	$1120.03 \pm 14.19$	$161.88 \pm 28.71$	0.013	$2.31 \pm 0.39$	2.82E+03
EVCC587	$1474.44 \pm 4.15$	$30.99 \pm 10.25$	0.002	$0.61 \pm 0.16$	1.25E+03
EVCC660	$1413.37 \pm 5.14$	$35.53 \pm 7.87$	0.028	$1.07 \pm 0.27$	8.60E+02
EVCC1223	$3030.06 \pm 4.62$	$28.73 \pm 7.14$	0.020	$0.61 \pm 0.17$	2.76E+03
EVCC176	$2208.29 \pm 9.02$	$122.29 \pm 21.35$	0.038	$4.95 \pm 0.73$	8.67E+03
EVCC231	$583.56 \pm 12.32$	$111.28 \pm 18.65$	0.016	$1.86 \pm 0.37$	1.55E+03
EVCC192	$2449.16 \pm 34.84$	$241.73 \pm 60.10$	0.005	$1.47 \pm 0.4$	3.98E+03
EVCC776	$2452.99 \pm 14.92$	$371.71 \pm 32.15$	0.015	$6.14 \pm 0.48$	3.47E+04
EVCC1209	$1236.47 \pm 14.35$	$98.69 \pm 29.70$	0.007	$0.76 \pm 0.21$	3.84E+02
EVCC451	$129.54 \pm 4.16$	$149.10 \pm 9.33$	0.03	$4.77 \pm 0.26$	3.98E+03

### 3.2 sed fitting

According to the Herschel and planck flux, the Spectral Energy Distribution (SED) of galaxies in the far infrared to submillimeter bands can be fitted. The sed fitting tool used in this paper is cigale. Code Investigating GALaxy Emission

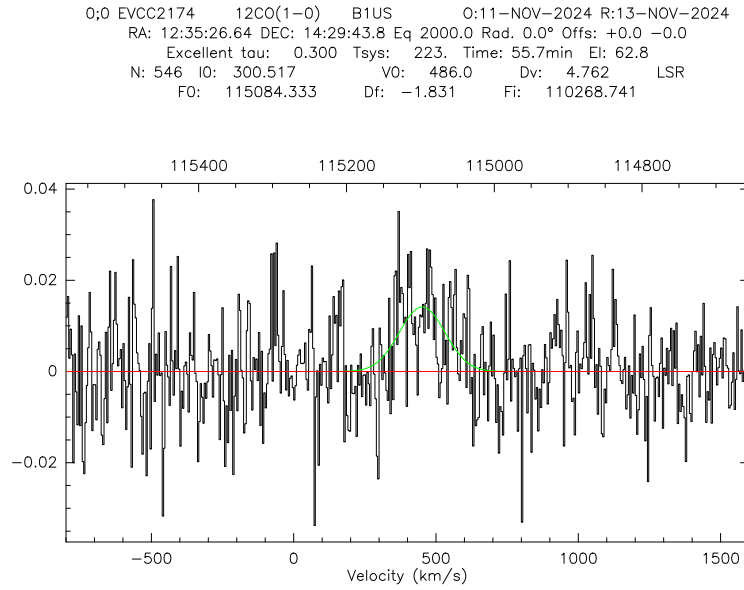
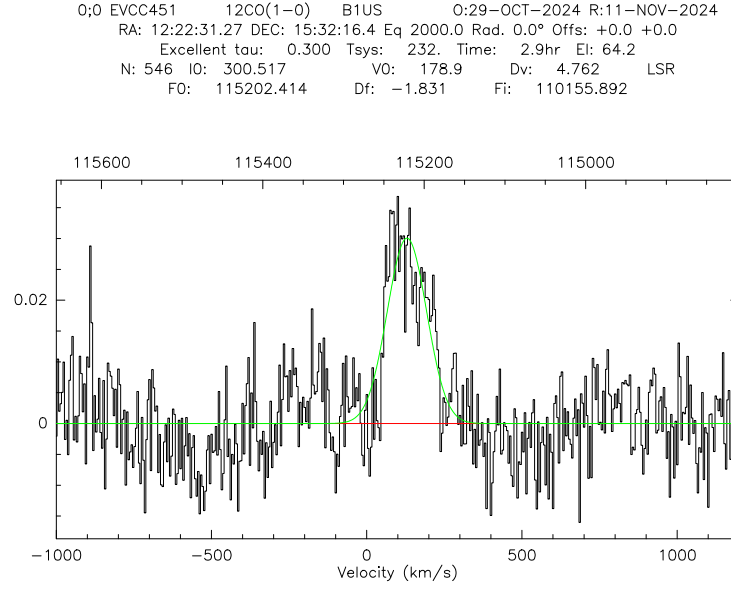
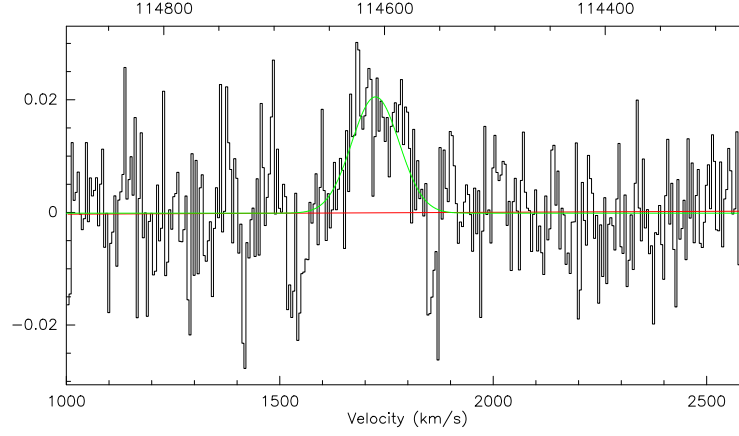


Figure 1: CO spectra of Virgo cluster galaxies.

0;0 EVCC2209 12CO(1-0) B1US 0:26-MAY-2024 R:03-JUL-2024  
 RA: 12:42:32.50 DEC: -00:04:50.5 Eq 2000.0 Rad. 0.0° Offs: -0.0 -0.0  
 Excellent tau: 0.300 Tsys: 274. Time: 86.3min El: 49.9  
 N: 546 I0: 300.517 V0: 1721. Dv: 4.762 LSR  
 F0: 114609.472 Df: -1.831 Fi: 110721.293



0;0 EVCC1104 12CO(1-0) B1US 0:07-SEP-2024 R:09-OCT-2024  
 RA: 12:43:50.95 DEC: -00:33:39.6 Eq 2000.0 Rad. 0.0° Offs: +0.8 -0.0  
 Excellent tau: 0.300 Tsys: 275. Time: 62.0min El: 45.3  
 N: 546 I0: 300.517 V0: 2631. Dv: 4.762 LSR  
 F0: 114259.766 Df: -1.831 Fi: 111055.207

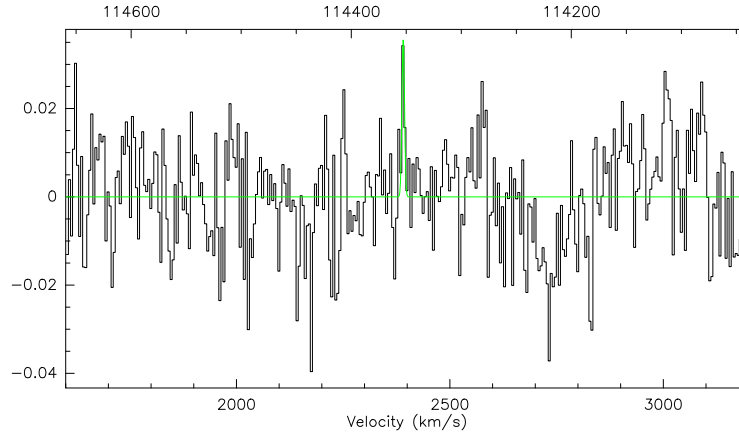
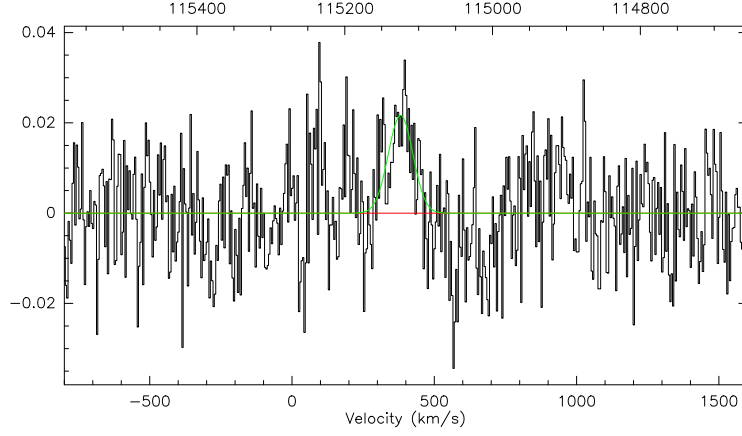


Figure 1: (continued)



0;0 EVCC171 12CO(1-0) B1US O:15-MAY-2024 R:29-OCT-2024  
RA: 12:12:46.18 DEC: 10:51:55.8 Eq 2000.0 Rad. 0.0° Offs: +0.0 +0.0  
Excellent tau: 0.300 Tsys: 268. Time: 64.7min El: 59.9  
N: 546 I0: 300.517 V0: 441.9 Dv: 4.762 LSR  
FO: 115101.290 Df: -1.831 Fi: 110251.736



0;0 EVCC2184 12CO(1-0) B1US O:11-MAY-2024 R:22-MAY-2024  
RA: 12:36:50.11 DEC: 13:09:55.1 Eq 2000.0 Rad. 0.0° Offs: +0.7 -0.0  
Excellent tau: 0.300 Tsys: 266. Time: 67.7min El: 64.7  
N: 327 I0: 180.510 V0: -235.0 Dv: 7.937 LSR  
FO: 115361.560 Df: -3.052 Fi: 110003.264

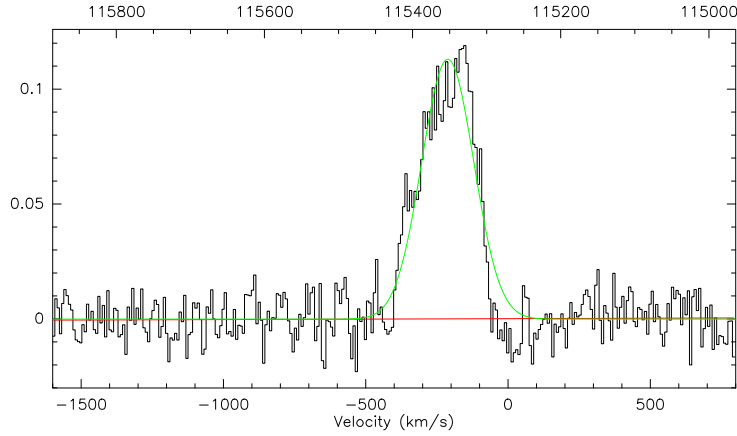
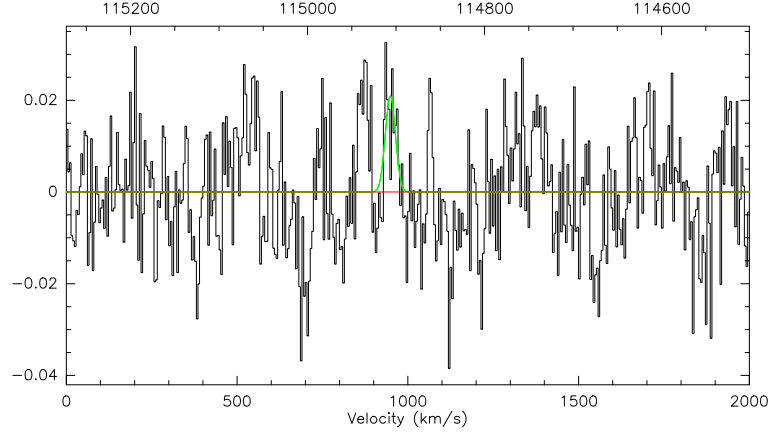


Figure 1: (continued)

0;0 EVCC488 12CO(1-0) B1US 0:29-JUN-2024 R:13-NOV-2024  
 RA: 12:23:38.76 DEC: 06:57:15.1 Eq 2000.0 Rad. 0.0° Offs: -0.0 -0.0  
 Excellent tau: 0.300 Tsys: 301. Time: 71.0min El: 57.7  
 N: 546 I0: 300.517 V0: 1000. Dv: 4.762 LSR  
 F0: 114886.699 Df: -1.831 Fi: 110456.543



0;0 EVCC884 12CO(1-0) B1US 0:06-JUN-2024 R:29-OCT-2024  
 RA: 12:34:03.05 DEC: 07:41:57.5 Eq 2000.0 Rad. 0.0° Offs: -0.0 -0.0  
 Excellent tau: 0.300 Tsys: 273. Time: 40.0min El: 59.0  
 N: 546 I0: 300.517 V0: 427.3 Dv: 4.762 LSR  
 F0: 115106.904 Df: -1.831 Fi: 110246.329

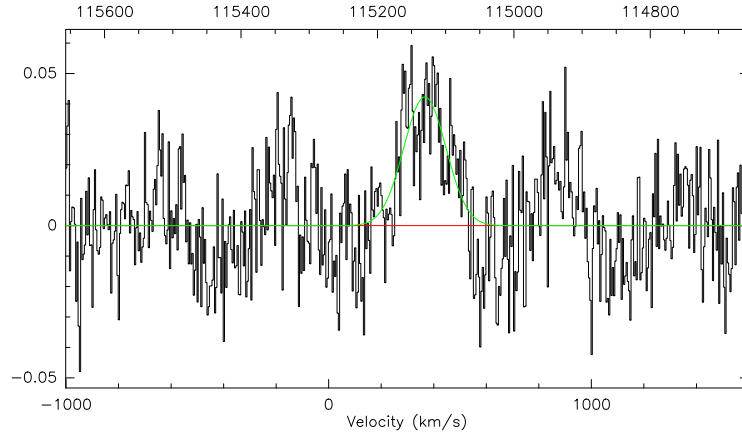
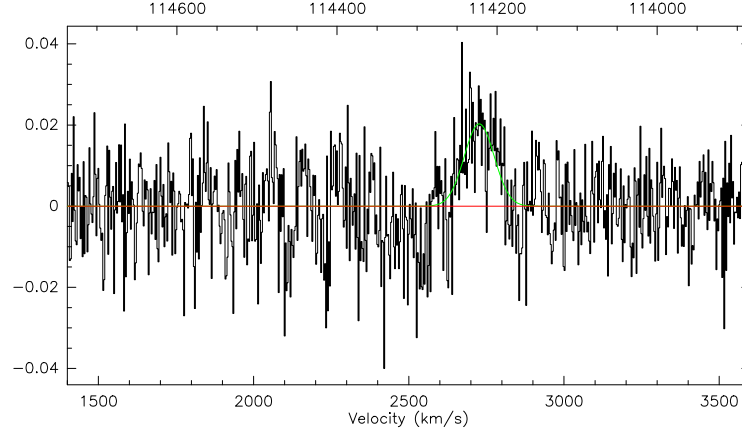


Figure 1: (continued)

0:0 EVCC1314 12CO(1-0) B1US 0:25-MAY-2024 R:24-DEC-2024  
 RA: 13:11:36.98 DEC: 22:54:55.4 Eq 2000.0 Rad. 0.0° Offs: +0.7 -0.0  
 Excellent tau: 0.300 Tsys: 283. Time: 2.0hr El: 46.1  
 N: 819 I0: 450.525 V0: 2622. Dv: 3.175 LSR  
 F0: 114262.842 Df: -1.221 Fi: 111052.256



0:0 EVCC231 12CO(1-0) B1US 0:27-SEP-2024 R:09-FEB-2025  
 RA: 12:15:30.36 DEC: 09:35:06.4 Eq 2000.0 Rad. 0.0° Offs: +0.8 -0.0  
 Excellent tau: 0.300 Tsys: 268. Time: 69.0min El: 48.3  
 N: 546 I0: 300.517 V0: 637.9 Dv: 4.762 LSR  
 F0: 115025.927 Df: -1.831 Fi: 110324.134

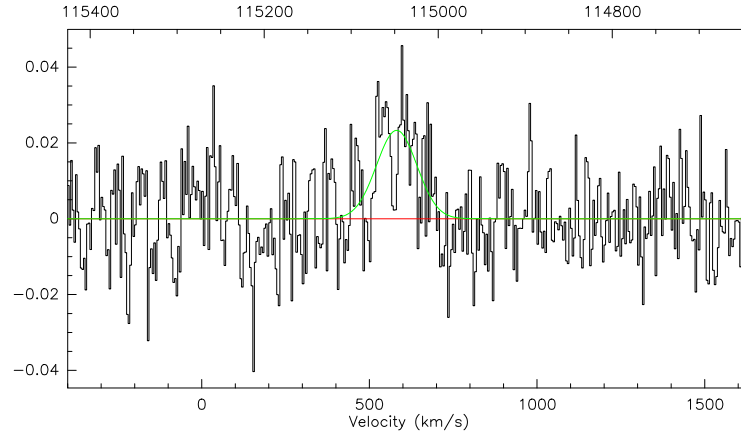
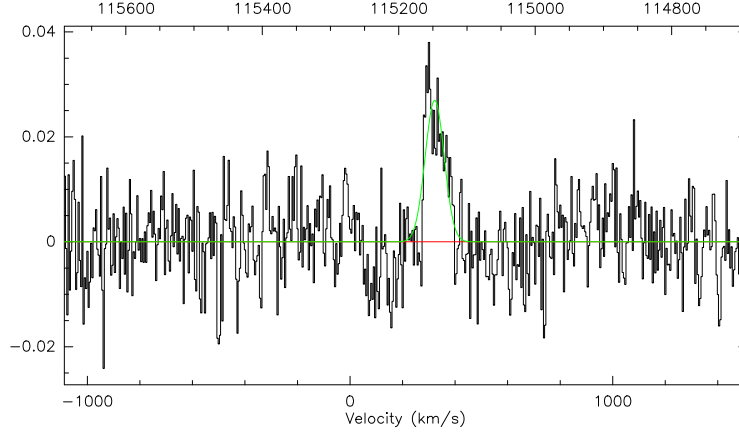


Figure 1: (continued)

0;0 EVCC952 12CO(1-0) B1US 0:02-NOV-2024 R:15-NOV-2024  
 RA: 12:36:56.28 DEC: 14:13:04.1 Eq 2000.0 Rad. 0.0° Offs: -0.0 -0.0  
 Excellent tau: 0.300 Tsys: 223. Time: 2.1hr El: 62.9  
 N: 546 I0: 300.517 V0: 340.8 Dv: 4.762 LSR  
 F0: 115140.163 Df: -1.831 Fi: 110215.362



0;0 EVCC84 12CO(1-0) B1US 0:29-MAY-2024 R:03-JUL-2024  
 RA: 12:02:42.26 DEC: 01:58:37.6 Eq 2000.0 Rad. 0.0° Offs: +0.8 +0.0  
 Excellent tau: 0.300 Tsys: 285. Time: 41.0min El: 53.5  
 N: 546 I0: 300.517 V0: 1997. Dv: 4.762 LSR  
 F0: 114503.387 Df: -1.831 Fi: 110822.435

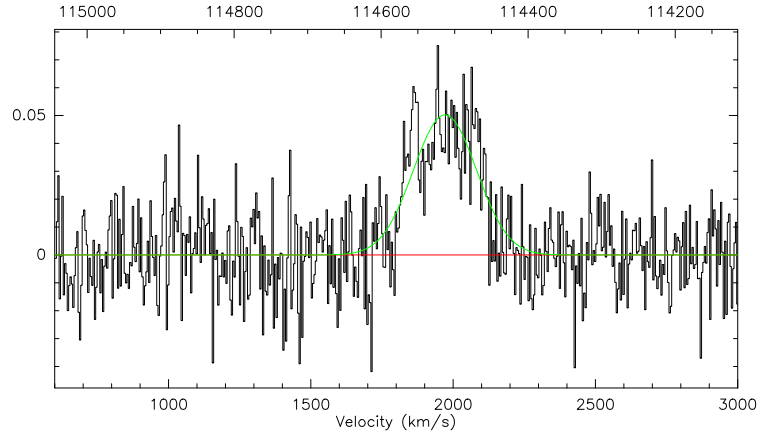
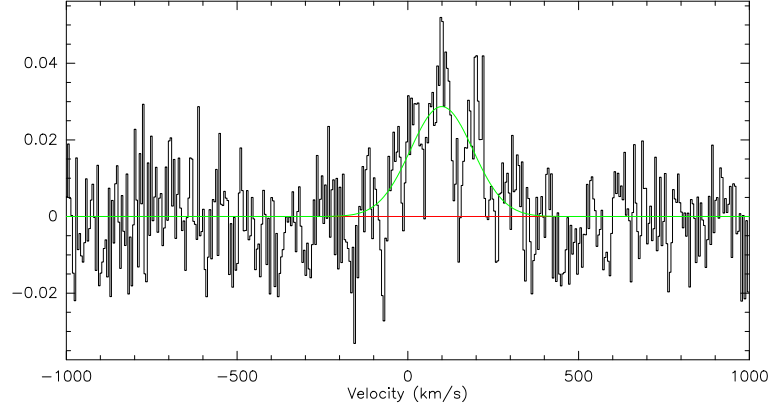


Figure 1: (continued)

0;0 EVCC1074 12CO(1-0) B1US O:11-JUN-2024 R:04-JUL-2024  
 RA: 12:42:40.92 DEC: 14:17:44.2 Eq 2000.0 Rad. 0.0° Offs: -0.0 -0.0  
 Excellent tau: 0.300 Tsys: 287. Time: 92.0min El: 57.4  
 N: 546 I0: 300.517 V0: 232.6 Dv: 4.762 LSR  
 F0: 115181.767 Df: -1.831 Fi: 110174.894



0;0 EVCC1282 12CO(1-0) B1US O:16-AUG-2024 R:09-OCT-2024  
 RA: 13:00:58.58 DEC: -00:01:39.7 Eq 2000.0 Rad. 0.0° Offs: -1.2 -1.5  
 Excellent tau: 0.300 Tsys: 289. Time: 65.7min El: 48.1  
 N: 546 I0: 300.517 V0: 1189. Dv: 4.762 LSR  
 F0: 114814.181 Df: -1.831 Fi: 110525.917

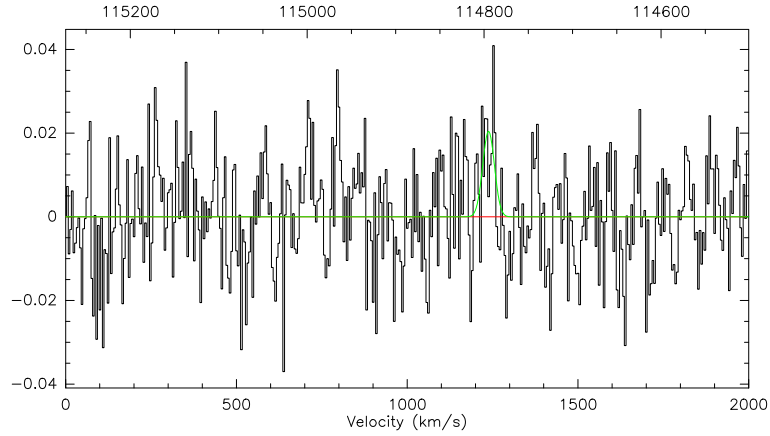


Figure 1: (continued)

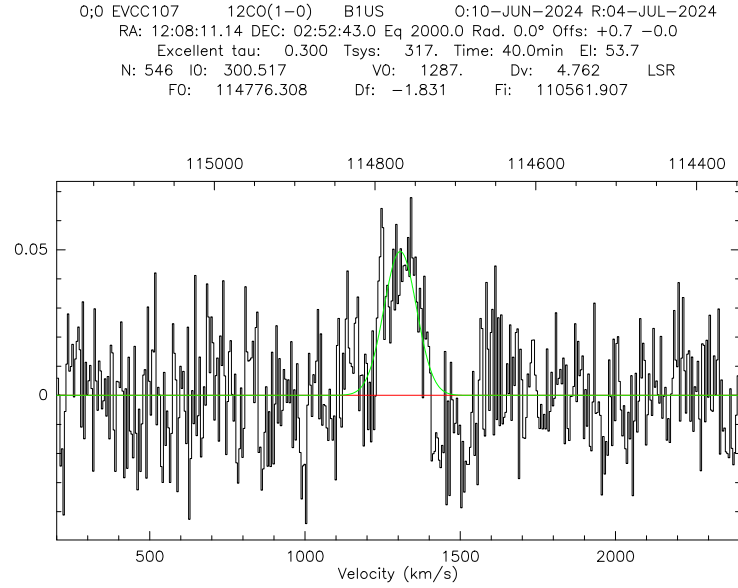
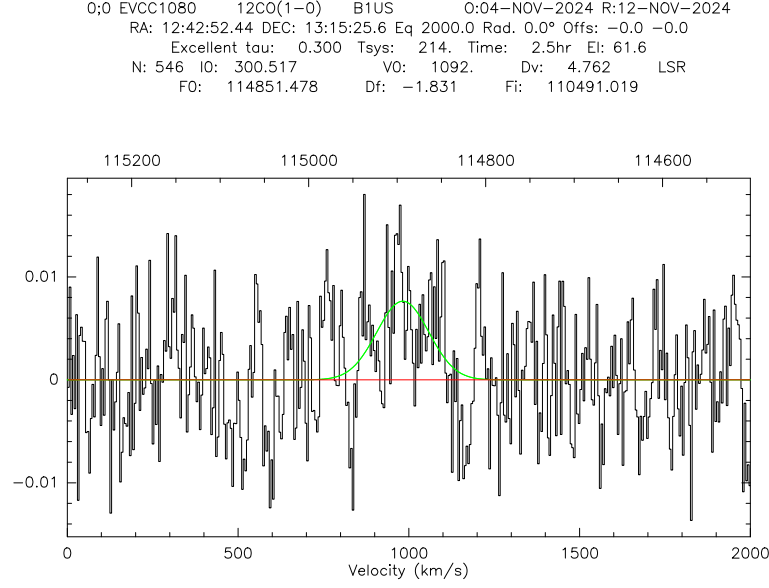
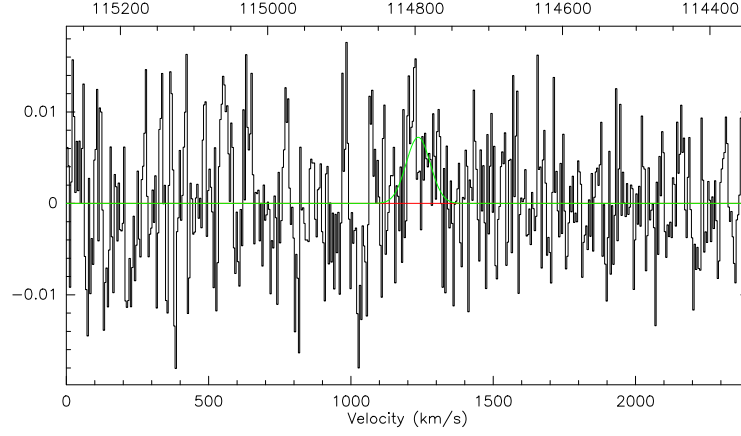


Figure 1: (continued)

0;0 EVCC1209 12CO(1-0) B1US 0:22-OCT-2024 R:11-NOV-2024  
 RA: 12:52:44.30 DEC: 15:50:46.7 Eq 2000.0 Rad. 0.0° Offs: +0.7 -0.0  
 Excellent tau: 0.300 Tsys: 205. Time: 2.0hr El: 65.9  
 N: 546 I0: 300.517 V0: 1306. Dv: 4.762 LSR  
 F0: 114768.964 Df: -1.831 Fi: 110569.694



0;0 EVCC1202 12CO(1-0) B1US 0:18-JUN-2024 R:04-JUL-2024  
 RA: 12:51:55.22 DEC: 12:04:58.8 Eq 2000.0 Rad. 0.0° Offs: +0.0 +0.0  
 Excellent tau: 0.300 Tsys: 280. Time: 83.3min El: 57.9  
 N: 546 I0: 300.517 V0: 1755. Dv: 4.762 LSR  
 F0: 114596.476 Df: -1.831 Fi: 110733.690

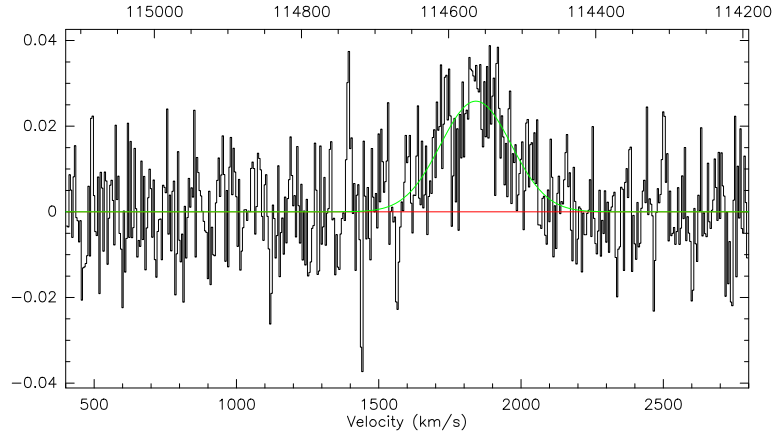
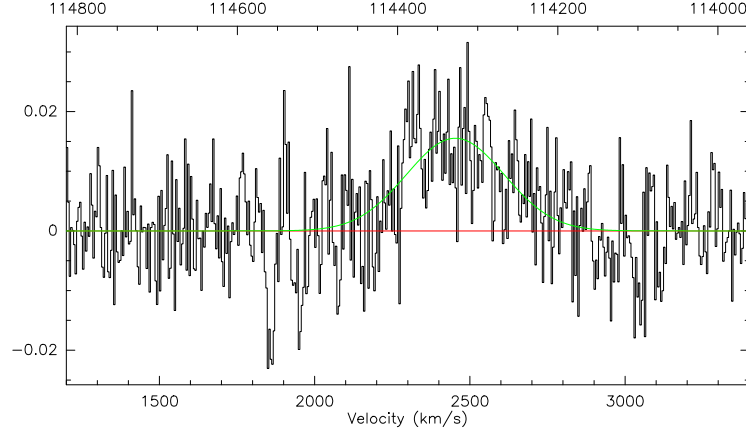


Figure 1: (continued)

0;0 EVCC776 12CO(1-0) B1US O:23-OCT-2024 R:08-NOV-2024  
RA: 12:30:26.76 DEC: 04:14:46.7 Eq 2000.0 Rad. 0.0° Offs: -0.0 -0.0  
Excellent tau: 0.300 Tsys: 200. Time: 80.0min El: 53.6  
N: 546 I0: 300.517 V0: 2443. Dv: 4.762 LSR  
FO: 114331.937 Df: -1.831 Fi: 110986.758



0;0 EVCC59 12CO(1-0) B1US O:16-JUN-2024 R:04-JUL-2024  
RA: 11:55:57.19 DEC: 06:44:55.3 Eq 2000.0 Rad. 0.0° Offs: +0.8 +0.0  
Excellent tau: 0.300 Tsys: 294. Time: 97.0min El: 47.2  
N: 546 I0: 300.517 V0: 2695. Dv: 4.762 LSR  
FO: 114234.812 Df: -1.831 Fi: 111078.724

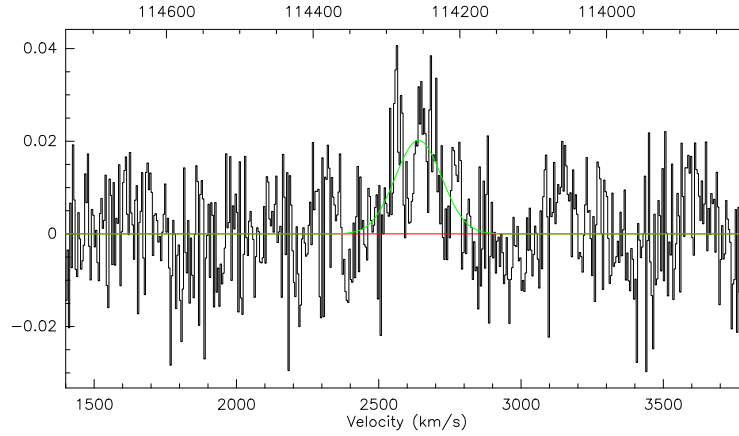
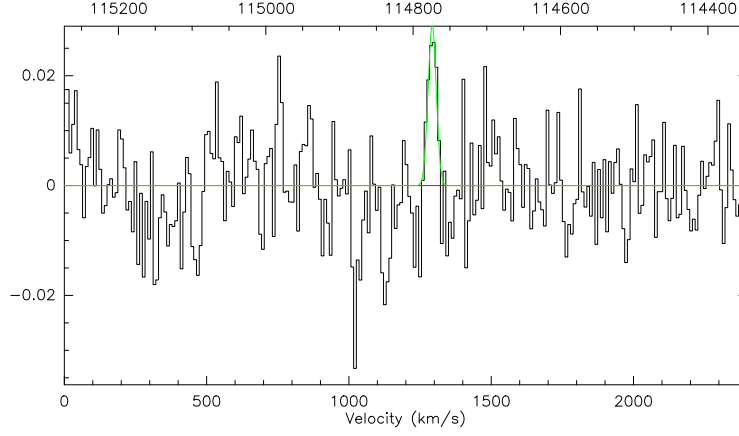


Figure 1: (continued)



0:0 EVCC104 12CO(1-0) B1US O:25-JUN-2024 R:04-JUL-2024  
 RA: 12:07:37.10 DEC: 02:41:28.3 Eq 2000.0 Rad. 0.0° Offs: -0.0 +0.0  
 Excellent tau: 0.300 Tsys: 326. Time: 1.7hr El: 48.5  
 N: 273 I0: 150.508 V0: 1331. Dv: 9.524 LSR  
 F0: 114759.313 Df: -3.662 Fi: 110578.116



0:0 EVCC631 12CO(1-0) B1US O:24-JUN-2024 R:05-JUL-2024  
 RA: 12:26:54.62 DEC: -00:52:39.4 Eq 2000.0 Rad. 0.0° Offs: +0.7 -0.0  
 Excellent tau: 0.300 Tsys: 292. Time: 84.7min El: 46.4  
 N: 546 I0: 300.517 V0: 2123. Dv: 4.762 LSR  
 F0: 114454.863 Df: -1.831 Fi: 110868.730

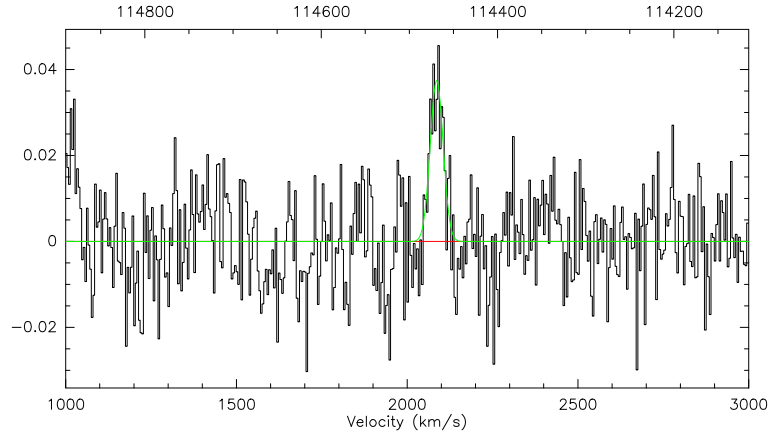


Figure 1: (continued)

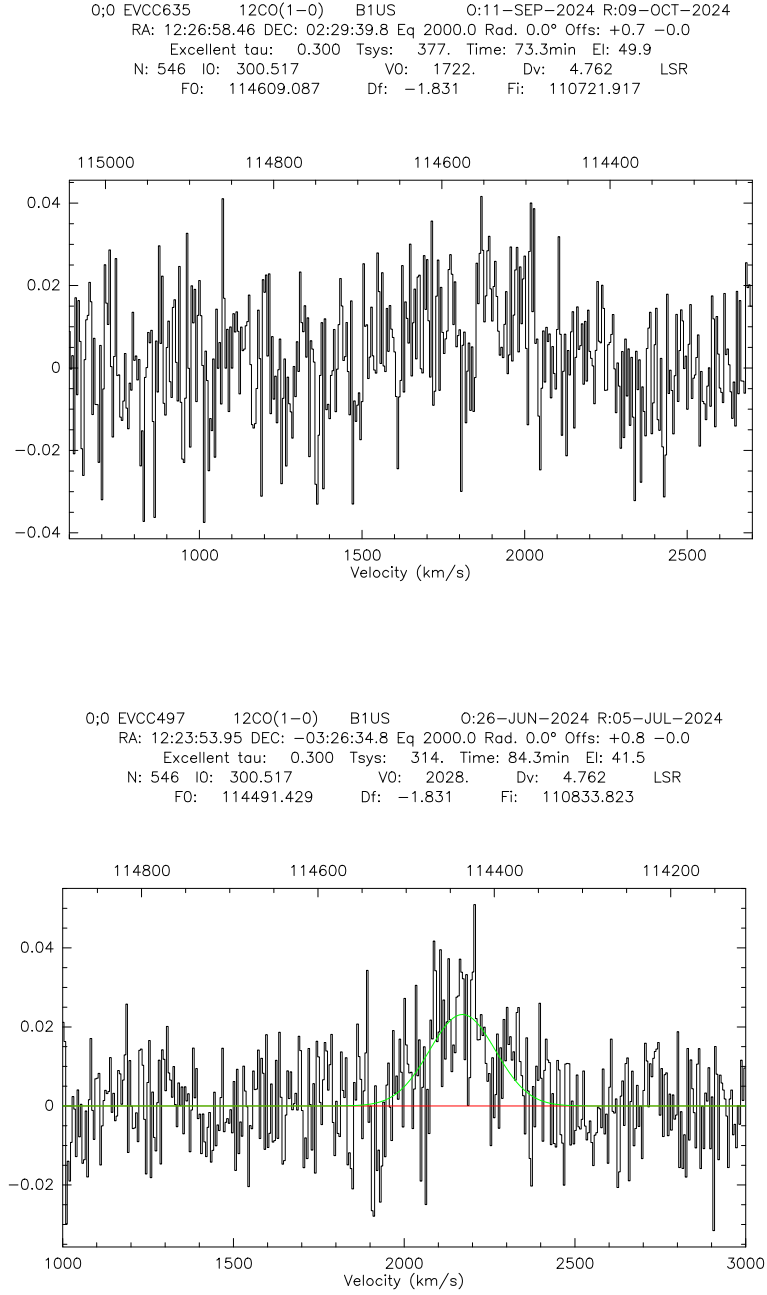
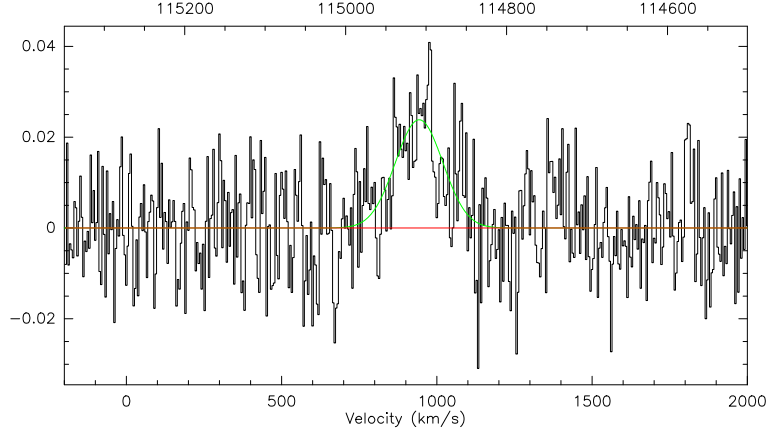


Figure 1: (continued)

0:0 EVCC574 12CO(1-0) B1US 0:14-JUN-2024 R:29-OCT-2024  
 RA: 12:25:42.48 DEC: 07:13:05.2 Eq 2000.0 Rad. 0.0° Offs: +0.7 -0.0  
 Excellent tau: 0.300 Tsys: 281. Time: 86.7min El: 54.7  
 N: 546 I0: 300.517 V0: 1002. Dv: 4.762 LSR  
 F0: 114885.814 Df: -1.831 Fi: 110457.391



0:0 EVCC153 12CO(1-0) B1US 0:06-JUN-2024 R:03-JUL-2024  
 RA: 12:11:52.56 DEC: 24:07:23.9 Eq 2000.0 Rad. 0.0° Offs: +0.0 +0.0  
 Excellent tau: 0.300 Tsys: 260. Time: 66.7min El: 55.3  
 N: 546 I0: 300.517 V0: 2688. Dv: 4.762 LSR  
 F0: 114237.619 Df: -1.831 Fi: 111076.166

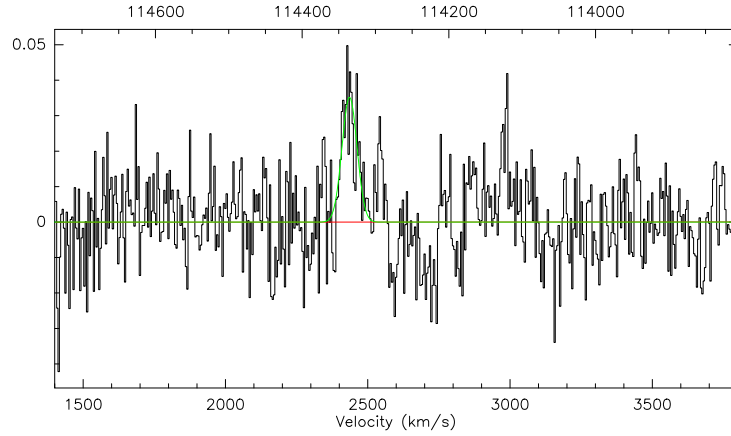
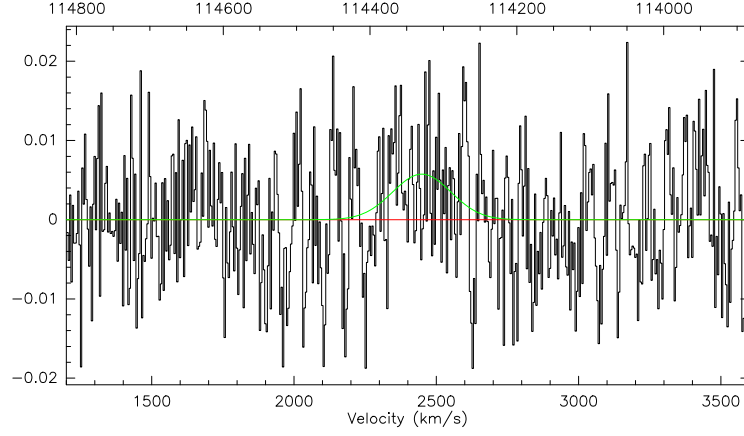


Figure 1: (continued)

0;0 EVCC192 12CO(1-0) B1US 0:28-OCT-2024 R:11-NOV-2024  
 RA: 12:13:53.62 DEC: 13:10:21.7 Eq 2000.0 Rad. 0.0° Offs: -0.0 +0.0  
 Excellent tau: 0.300 Tsys: 206. Time: 74.7min El: 58.0  
 N: 546 I0: 300.517 V0: 2464. Dv: 4.762 LSR  
 F0: 114323.747 Df: -1.831 Fi: 110994.685



0;0 EVCC1099 12CO(1-0) B1US 0:20-MAY-2024 R:23-MAY-2024  
 RA: 12:43:32.76 DEC: 11:34:51.2 Eq 2000.0 Rad. 0.0° Offs: -0.0 -0.0  
 Excellent tau: 0.300 Tsys: 292. Time: 38.3min El: 41.5  
 N: 546 I0: 300.517 V0: 1417. Dv: 4.762 LSR  
 F0: 114726.284 Df: -1.831 Fi: 110609.835

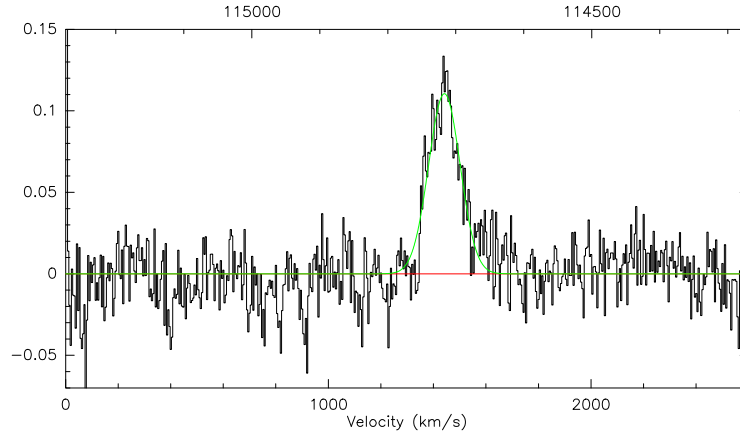


Figure 1: (continued)

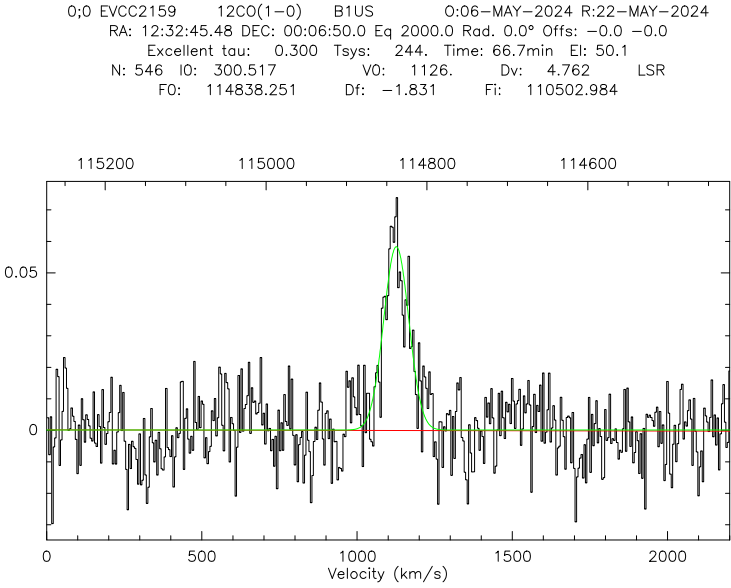
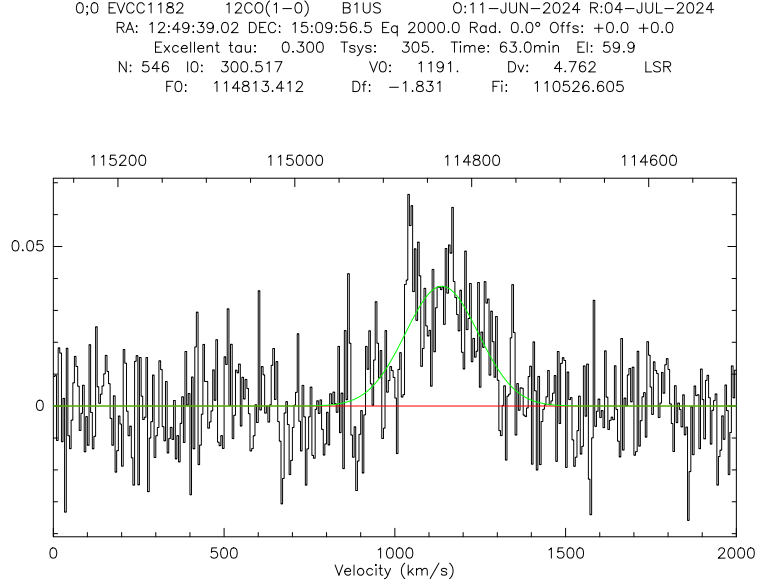
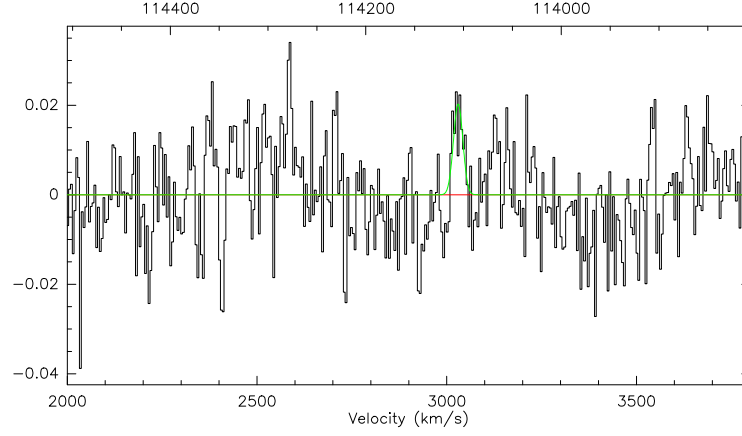


Figure 1: (continued)

0;0 EVCC1223 12CO(1-0) B1US 0:29-AUG-2024 R:09-OCT-2024  
RA: 12:53:50.83 DEC: 09:42:36.4 Eq 2000.0 Rad. 0.0° Offs: +0.8 -0.0  
Excellent tau: 0.300 Tsys: 304. Time: 93.3min El: 57.2  
N: 546 I0: 300.517 V0: 2861. Dv: 4.762 LSR  
FO: 114171.176 Df: -1.831 Fi: 111139.761



0;0 EVCC952 12CO(1-0) B1US 0:02-NOV-2024 R:15-NOV-2024  
RA: 12:36:56.28 DEC: 14:13:04.1 Eq 2000.0 Rad. 0.0° Offs: -0.0 -0.0  
Excellent tau: 0.300 Tsys: 223. Time: 2.1hr El: 62.9  
N: 546 I0: 300.517 V0: 340.8 Dv: 4.762 LSR  
FO: 115140.163 Df: -1.831 Fi: 110215.362

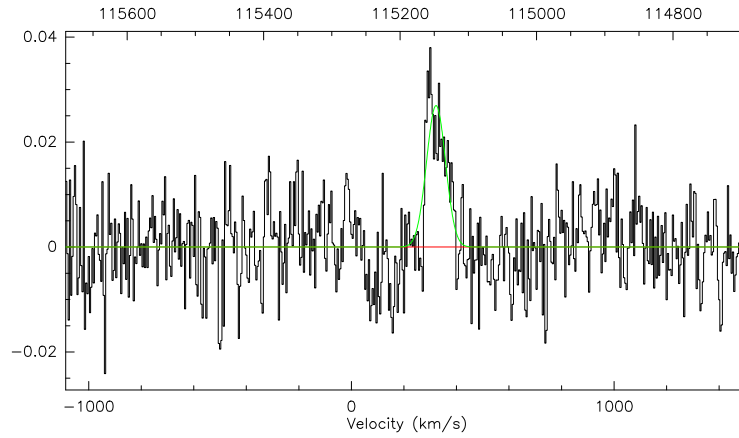


Figure 1: (continued)

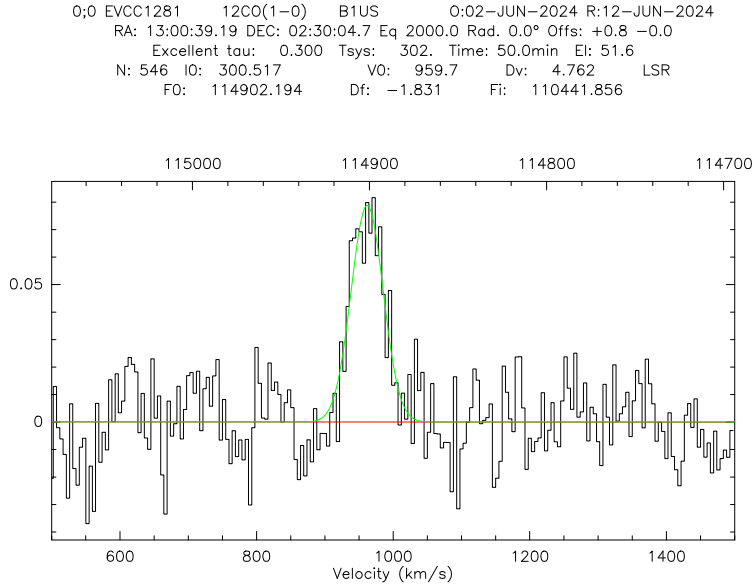
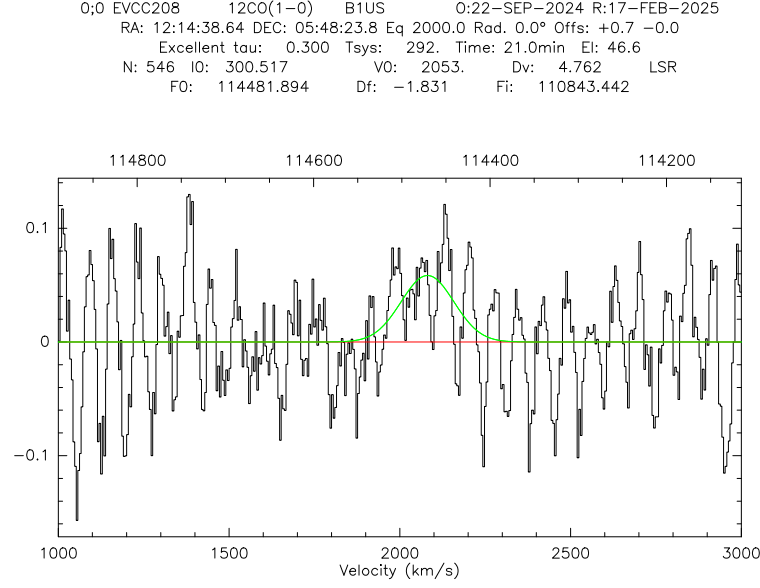
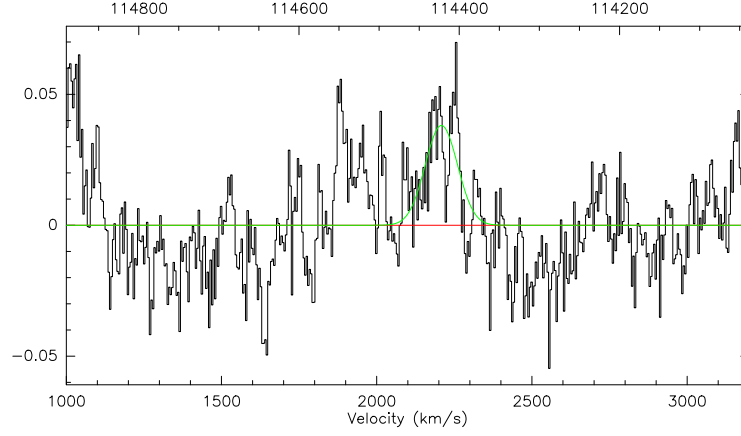


Figure 1: (continued)

0;0 EVCC176 12CO(1-0) B1US 0:21-SEP-2024 R:10-OCT-2024  
 RA: 12:13:03.05 DEC: 07:02:20.0 Eq 2000.0 Rad. 0.0° Offs: -0.0 +0.0  
 Excellent tau: 0.300 Tsys: 352. Time: 2.0hr El: 45.7  
 N: 546 I0: 300.517 V0: 2263. Dv: 4.762 LSR  
 F0: 114401.071 Df: -1.831 Fi: 110920.545



0;0 EVCC208 12CO(1-0) B1US 0:22-SEP-2024 R:17-FEB-2025  
 RA: 12:14:38.64 DEC: 05:48:23.8 Eq 2000.0 Rad. 0.0° Offs: +0.7 -0.0  
 Excellent tau: 0.300 Tsys: 292. Time: 21.0min El: 46.6  
 N: 546 I0: 300.517 V0: 2053. Dv: 4.762 LSR  
 F0: 114481.894 Df: -1.831 Fi: 110843.442

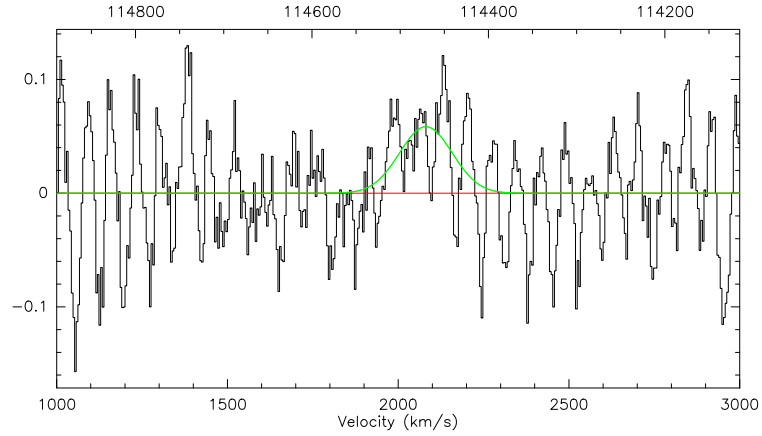
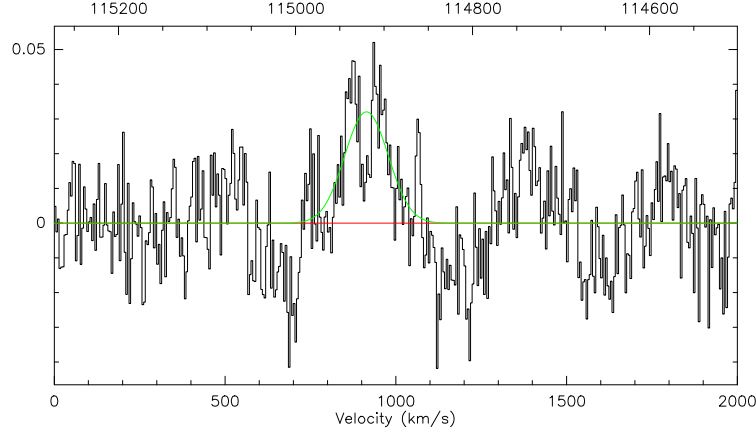


Figure 1: (continued)



0;0 EVCC488 12CO(1-0) B1US 0:29-JUN-2024 R:07-FEB-2025  
 RA: 12:23:38.76 DEC: 06:57:15.1 Eq 2000.0 Rad. 0.0° Offs: -0.0 -0.0  
 Excellent tau: 0.300 Tsys: 301. Time: 71.0min El: 57.7  
 N: 546 I0: 300.517 V0: 1000. Dv: 4.762 LSR  
 F0: 114886.699 Df: -1.831 Fi: 110456.543



0;0 EVCC808 12CO(1-0) B1US 0:25-MAY-2024 R:03-JUL-2024  
 RA: 12:31:39.29 DEC: 03:56:23.6 Eq 2000.0 Rad. 0.0° Offs: +0.0 +0.0  
 Excellent tau: 0.300 Tsys: 257. Time: 72.7min El: 52.6  
 N: 546 I0: 300.517 V0: 1746. Dv: 4.762 LSR  
 F0: 114599.705 Df: -1.831 Fi: 110730.601

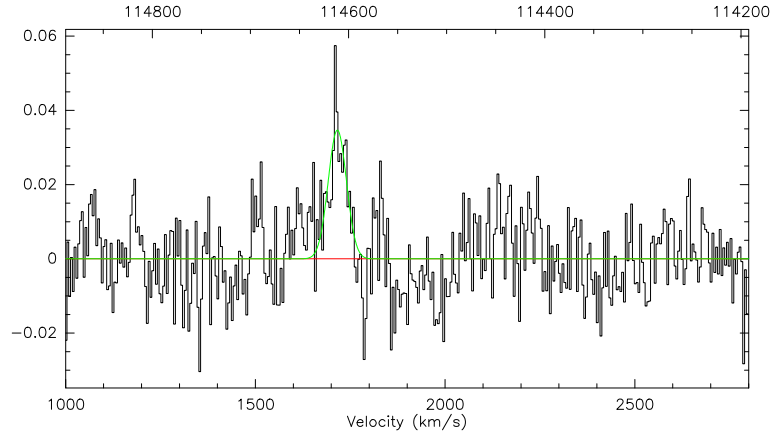
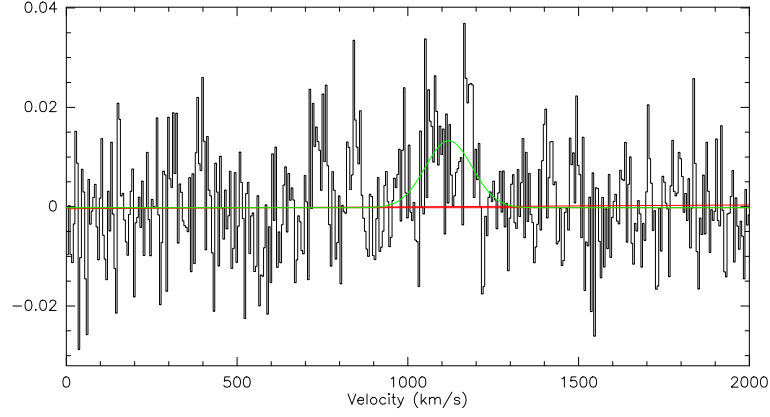


Figure 1: (continued)

0;0 EVCC1217 12CO(1-0) B1US 0:22-AUG-2024 R:09-OCT-2024  
 RA: 12:53:21.22 DEC: 01:16:09.1 Eq 2000.0 Rad. 0.0° Offs: +0.0 -0.0  
 Excellent tau: 0.300 Tsys: 321. Time: 1.9hr El: 48.8  
 N: 546 I0: 300.517 V0: 1125. Dv: 4.762 LSR  
 F0: 114838.482 Df: -1.831 Fi: 110502.747



0;0 EVCC461 12CO(1-0) B1US 0:26-JUN-2024 R:05-JUL-2024  
 RA: 12:22:42.22 DEC: 09:19:57.7 Eq 2000.0 Rad. 0.0° Offs: +0.7 -0.0  
 Excellent tau: 0.300 Tsys: 273. Time: 2.2hr El: 57.3  
 N: 546 I0: 300.517 V0: 1249. Dv: 4.762 LSR  
 F0: 114791.111 Df: -1.831 Fi: 110547.808

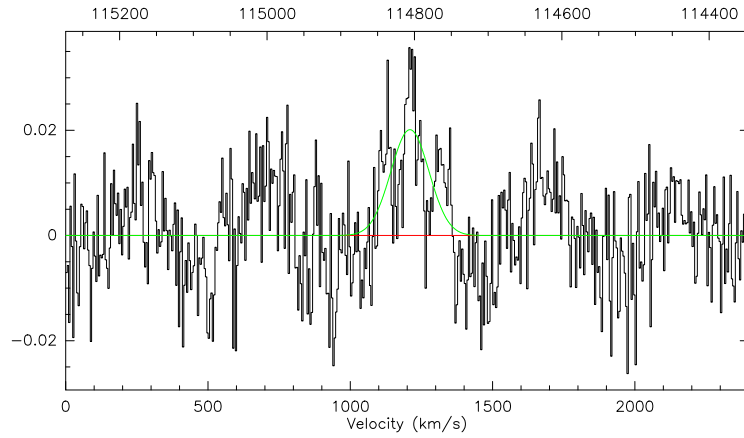


Figure 1: (continued)

(CIGALE) is a Python code for the fitting of spectral energy distribution (SED) of galaxies<sup>3</sup>. It has been developed for more than 1.5 decades (e.g. Burgarella et al. 2005; Noll et al. 2009; Boquien et al. 2019).

cigale can use different dust models and empirical templates to trace dust emission and thus synthesize a galaxy's sed. The emission of stars and dust is related to dust decay, which is estimated by taking into account the energy balance between the energy emitted by the different populations of stars absorbed by the dust and the energy re-emitted in the infrared. The model spectra are constructed assuming different star formation histories, metallicity, and decay laws. They are then convolved with transmissivity profiles of different photometric bands commonly used for space missions and compared with multi-frequency observations. The code determines the best fit model by  $\chi^2$  minimization and performs a probability distribution function (PDF) analysis to determine the weighted mean and standard deviation of different physical parameters such as star mass and star formation rate.

Our template for using the cigale model is the cigale model of galaxy clusters in Boselli & Roehlly et al. 2016, which, in addition to the Herschel and Planck data, Four bands irsa (Wheelock & Gautier III et al. 2019) 16, 25, 100, 160 were also added in order to have more data points to make the fitting of the model more accurate. Table 4 shows the data points for seed fitting with cigale and the simulated total IR luminosity and SFH.

Table 4: Properties of the Virgo

EVCC	$\log(M_{H_2})$ $M_\odot$	$M_{H_2}$	$M_{HI}$	$\text{def}_{HI}$	Hflux $Jy \text{ km s}^{-1}$	$t_{\text{gas}}$	$t_{M_{H_2}}$	$t_{M_{HI}}$
EVCC429	8.75E+00	3.34E+08	1.17E+10	-0.503	84.71	1.38E+09	3.81E+07	1.34E+09
EVCC2159	3.80E+00	1.12E+08	2.06E+09	0.411	126.55	5.72E+08	2.96E+07	5.42E+08
EVCC2184	3.38E+00	2.00E+09	7.34E+08	0.974	11.15	8.07E+08	5.90E+08	2.17E+08
EVCC1099	2.28E+00	5.63E+08	5.17E+08	0.723	7.86	4.73E+08	2.47E+08	2.27E+08
EVCC171	1.11E+00	1.65E+08	3.76E+09	0.173	62.20	3.52E+09	1.48E+08	3.37E+09
EVCC2174	8.20E-01	1.77E+08	5.41E+08	0.935	10.18	8.74E+08	2.15E+08	6.59E+08
EVCC233	2.46E+00	5.11E+08	9.16E+08	0.212	13.92	5.81E+08	2.08E+08	3.73E+08
EVCC808	1.22E+00	1.21E+08	2.15E+09	-0.132	43.41	1.87E+09	9.94E+07	1.77E+09
EVCC1314	7.81E-01	1.22E+09	6.25E+09	-0.131	14.67	9.56E+09	1.56E+09	8.00E+09
EVCC2209	1.20E+00	1.64E+08	2.14E+09	-0.227	43.68	1.91E+09	1.37E+08	1.78E+09
EVCC952	8.79E-01	1.87E+08	7.00E+08	0.526	10.63	1.01E+09	2.13E+08	7.96E+08
EVCC84	1.96E+00	4.38E+09	5.75E+09	-0.236	21.45	5.18E+09	2.24E+09	2.94E+09
EVCC884	1.58E+00	7.04E+08	1.41E+07	2.579	0.20	4.54E+08	4.45E+08	8.94E+06
EVCC1281	3.05E+00	3.59E+08	1.31E+09	0.191	19.71	5.48E+08	1.18E+08	4.30E+08
EVCC1074	1.69E+00	1.02E+09	5.00E+08	0.595	7.59	9.00E+08	6.04E+08	2.96E+08
EVCC107	2.25E+00	1.64E+09	6.64E+09	-0.427	53.69	3.69E+09	7.30E+08	2.96E+09
EVCC1202	2.97E+00	2.53E+09	4.72E+09	0.289	17.6	2.44E+09	8.52E+08	1.59E+09
EVCC1182	3.67E+00	6.80E+08	5.53E+07	1.893	0.84	2.00E+08	1.85E+08	1.51E+07
EVCC673	2.53E-01	2.66E+08	5.27E+08	0.955	8.01	3.13E+09	1.05E+09	2.08E+09
EVCC59	2.02E+00	1.54E+09	1.50E+10	-0.432	47.02	8.20E+09	7.63E+08	7.44E+09
EVCC104	1.72E+00	1.51E+08	4.90E+09	-0.390	39.92	2.94E+09	8.79E+07	2.85E+09
EVCC574	1.87E+00	6.61E+08	3.39E+09	0.001	27.42	2.17E+09	3.54E+08	1.82E+09
EVCC631	8.13E+00	1.38E+08					1.70E+07	
EVCC461	6.36E-01	4.90E+08	1.18E+09	0.413	9.55	2.63E+09	7.70E+08	1.86E+09
EVCC497	1.38E+00	4.38E+08					3.17E+08	
EVCC153	2.22E+00	1.24E+09	6.16E+09	-0.280	13.54	3.34E+09	5.57E+08	2.78E+09
EVCC488	3.31E-01		6.79E+08	0.494	5.49			2.06E+09
EVCC439	8.28E-01	1.78E+08	8.38E+07	1.655	1.32	3.16E+08	2.15E+08	1.01E+08
EVCC1080	6.68E-01	1.78E+08	1.98E+09	0.042	19.01	3.23E+09	2.66E+08	2.96E+09
EVCC126	2.07E+00	1.30E+08	1.73E+09	0.132	26.25	8.97E+08	6.29E+07	8.34E+08
EVCC1178	1.25E+00	2.60E+08	3.10E+09	-0.077	47.61	2.69E+09	2.09E+08	2.48E+09
EVCC1282	1.47E+00	7.62E+07	1.09E+09	0.023	14.63	7.98E+08	5.19E+07	7.46E+08
EVCC1217	8.46E-01	2.60E+08	1.13E+09	0.438	11.69	1.64E+09	3.08E+08	1.33E+09
EVCC996	1.67E+00							
EVCC587	1.43E-02	1.15E+08	7.34E+08	0.965	5.88	5.93E+10	8.04E+09	5.12E+10

<sup>3</sup><https://cigale.lam.fr/>

EVCC	$\log(M_{H_2})$ $M_\odot$	$M_{H_2}$	$M_{HI}$	$\text{def}_{HI}$	Hlflux $Jy\ km\ s^{-1}$	$t_{\text{gas}}$	$t_{M_{H_2}}$	$t_{M_{HI}}$
EVCC660	1.26E+00	7.95E+07	4.19E+08	0.701	6.61	3.95E+08	6.30E+07	3.32E+08
EVCC1223	8.07E-01	2.55E+08	3.15E+09	0.076	8.81	4.22E+09	3.16E+08	3.90E+09
EVCC1069	1.14E+00	4.90E+08		0.264	7.53			4.30E+08
EVCC1104	2.27E-01							
EVCC635	1.10E+00	8.02E+08		-0.070	14.91			7.27E+08
EVCC176	1.26E+00	8.01E+08	4.37E+08	0.784	3.16	9.85E+08	6.38E+08	3.48E+08
EVCC208	8.15E-01	1.65E+09		0.399	25.71			2.03E+09
EVCC231	1.06E+00	1.43E+08	4.32E+08	0.213	6.57	5.45E+08	1.36E+08	4.09E+08
EVCC1243	1.84E-01	1.08E+09		0.119	22.00			5.86E+09
EVCC192	8.93E-01	3.68E+08	1.80E+09	0.376	8.41	2.42E+09	4.12E+08	2.01E+09
EVCC776	3.29E-01	3.21E+09	5.05E+09	-0.093	11.31	2.51E+10	9.77E+09	1.54E+10
EVCC1209	1.01E+00	3.55E+07	5.21E+08	0.370	13.07	5.51E+08	3.51E+07	5.16E+08
EVCC451	7.45E-01	3.68E+08	1.27E+08	1.116	1.93	6.64E+08	4.93E+08	1.70E+08

## 4 Data analysis

### 4.1 CO Properties in Different Environments

#### 4.1.1 CO Properties as a Function of the Optical Parameters

We first investigated the relationship between the molecular gas and the optical properties of the galaxy, which is essential to minimize the possibility of confusing the properties of the inherent molecular gas with environmental influences.

First of all, Figure 2, Figure 3 and Figure 4 show the change of general properties of molecular gas with morphological type(LED A)<sup>4</sup>, B-band absolute magnitude(LED A) and K-band luminosity respectively(2MASS; Skrutskie & Cutri et al. 2006; Jarrett. 2000; Jarrett et al. 2003).

As can be seen from Figure 2, galaxies with polymer gas converge to the sb-sc type, but generally speaking, the content of molecular gas has no significant relationship with the form type of galaxies, and the relationship between the mass of molecular gas and the form type is consistent with previous studies(e.g., Young & Scoville 1991; Chung et al. 2017).

In Figure 3, we can see that the mass of the molecular gas increases with the increase of the absolute magnitude of the B-band, but the scattering is larger. In Figure 3, we can see that the mass of the molecular gas is roughly linear with the luminosity of the K band, which is consistent with previous studies by others.(Chung et al. 2017; Lisenfeld et al. 2011)

### 4.2 CO and HI

HI gas is typically the most vulnerable component in a galaxy, since it extends far beyond the optical size and is thus weakly bound by gravity.(e.g., Hewitt et al. 1983). As such, it is vulnerable to any external force, and can often serve as a useful tool for studying how galaxies interact with their surroundings (e.g., Hibbard et al. 2001; Chung et al. 2009a). By comparing molecular gas content and HI defects, we can better understand the gas composition of galaxies, the star formation process, and the physical mechanisms of galactic evolution. In this section, the relationship between CO luminosity normalized by K band luminosity and HI defect  $\text{def}_{HI}$  is studied.

In Figure 5, we plot the relationship between co luminosity normalized with K-band luminosity and  $\text{def}_{HI}$ . As can be seen from the figure, the ratio of  $L_{CO}/L_K$  decreases with increasing  $\text{def}_{HI}$ , indicating that galaxies lacking HI are also lacking molecular gas, which is consistent with previous findings (Chung et al. 2017).

### 4.3 Star Formation Rates and Gas

For star formation activity in galaxies in Virgo clusters, this study examined the total radiant heat star formation rate (sed-fitting, section 3.2). The average disk star formation rate per unit area ( $\sum SFR = SFR/diskarea$ ) is expressed as a function of  $\text{def}_{HI}$  and  $\log L_{CO}/L_K$ , as shown in Figure 6. The Virgo clusters galaxy shows  $\sum SFR \sim 10^{-3} - 10^{-2} M_\odot yr^{-1} KPC^{-2}$ .

<sup>4</sup><http://atlas.obs-hp.fr/hyperleda/ledacat.cgi?o=EVCC%203>

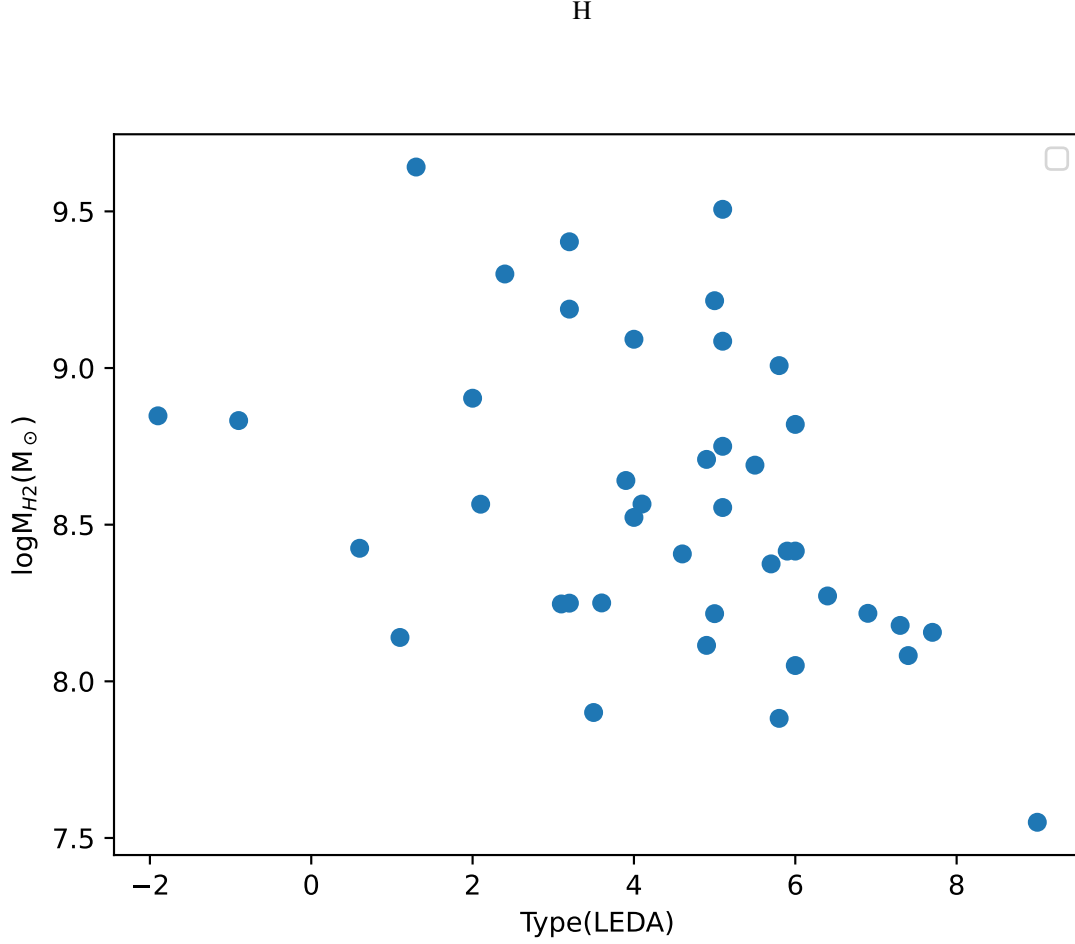


Figure 2: Molecular gas mass as a function of the morphological type

The strong correlation between  $\sum SFR$  and gas can be seen from the comparison of  $\sum SFR$  and gas in Figure 6, and in the left figure we can see that galaxies with higher CO content in Virgo clusters have higher  $\sum SFR$ . In the comparison of  $def_{HI}$  and  $\sum SFR$  in the graph on the right, galaxies with high  $\sum SFR$  are mostly in normal HI-rich galaxies, while galaxies with poor HI have low  $\sum SFR$  activity. This is consistent with our theory and previous research.

#### 4.4 Gas dissipation time

The Kennicutt-Schmidt relationship (Kennicutt, 1998, 1989) shows that molecular gas and star formation are extremely closely linked across a wide range of galaxy types, both in the local universe and in high redshift galaxy types. The ratio of molecular mass to the rate of star formation, known as gas dissipation time, measures the time scale of molecular gas depletion, that is, the amount of time a galaxy can sustain star formation at its current rate without accreting gas. The gas dissipation mass used in this paper is: the time required for a galaxy to consume all of its cold gas through star formation. The gas mass and star formation rate (It is obtained in the 2.1 by fitting the galaxy) used are calculated as follows:

$$t^{gas}(yr) = \frac{SFR(M_{\odot} yr^{-1})}{M_{gas}}$$

where SFR is the star formation rate,  $M_{gas}$  is the H I, H<sub>2</sub> and the total gas mass. Figure 7, Figure 8 and Figure 9 show the relationship between atomic, molecular and total gas dissipation time and  $def_{HI}$  and  $L_{CO}/L_K$  respectively. The atomic and molecular gas consumption time ranges from 0.1-16 Gyr and 0.2-2.5 Gyr, respectively.

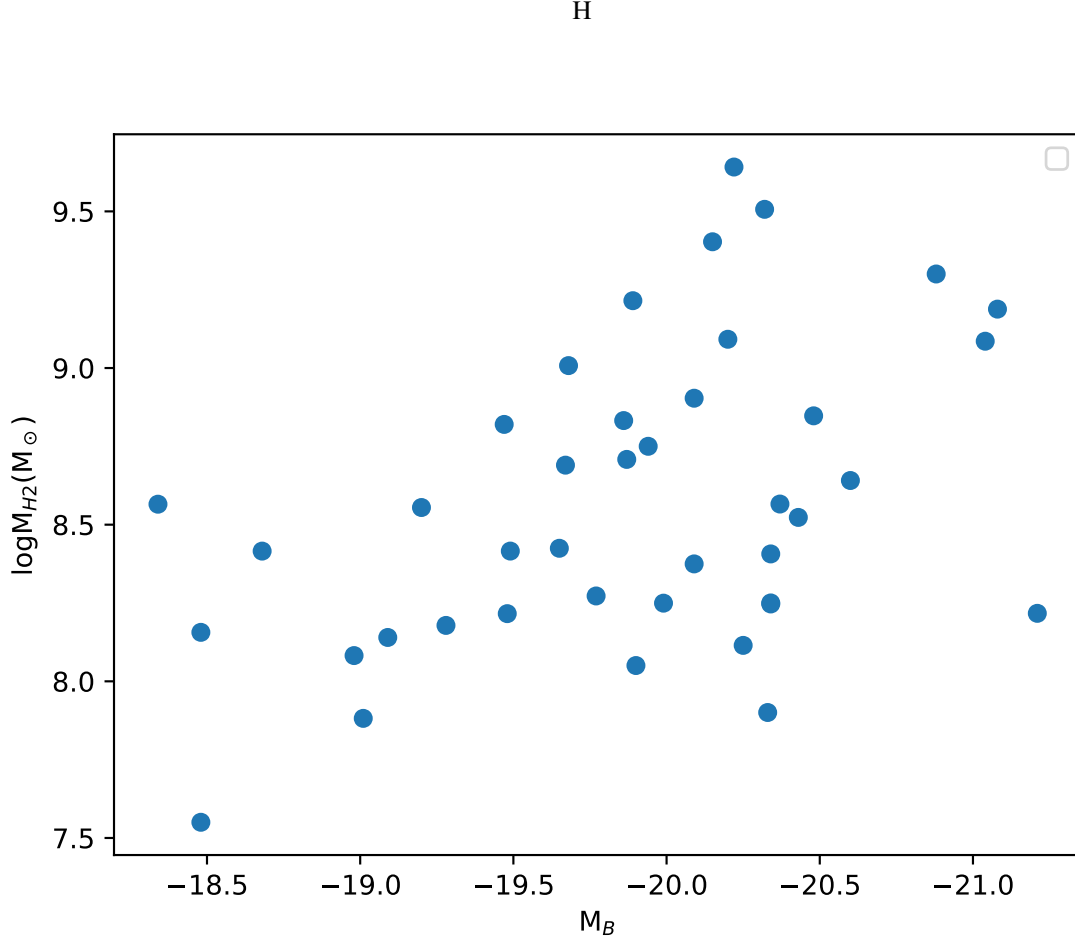


Figure 3: The corrected optical B-magnitude

The ratio of  $H_2$  to  $\text{def}_{HI}$  in Figure 7 shows that  $t^{H_2}$  seems to increase with the increase of  $\text{def}_{HI}$  when there is no shortage of HI gas, but  $t^{H_2}$  seems to decrease with the increase of  $\text{def}_{HI}$  when there is the greatest shortage of HI. This can also prove that the efficiency of star formation is directly related to the dissipation time of molecular gas, and the lack of HI may be related to the rapid dissipation of gas during star formation.

In Figure 8, we see that the dissipation time of atomic gas is inversely related to  $\text{def}_{HI}$ , and it can be seen that although the star formation rate and the atomic gas mass tend to be smaller in HI deficient galaxies, the lost hydrogen gas seems to have a stronger effect, resulting in an inverse correlation between the atomic gas consumption time and the HI deficient galaxies.

In Figure 9, the total cold air ( $HI + H_2$ ) consumption time of the whole sample has a slightly decreasing trend with the increase of  $\text{def}_{HI}$ . The total cold gas consumption time is relatively insensitive compared to the distribution of total cold gas mass or SFR, which may reflect the highly local and short time scales associated with star formation activity. The more prominent trend in molecular gas consumption time compared to atomic or total gas consumption time suggests that internal processes are more important than external, ICM-driven processes and can explain the overall trend observed here.

For the ratio of  $L_{CO}$  normalized with K-band luminosity to the dissipation time of the gas, whether it is the dissipation time of molecules, atoms and total cold gas. Both of them increase with the increase of  $L_{CO}/L_K$ , indicating that  $L_{CO}/L_K$  can be a good standard to measure the dissipation time of cold gas.

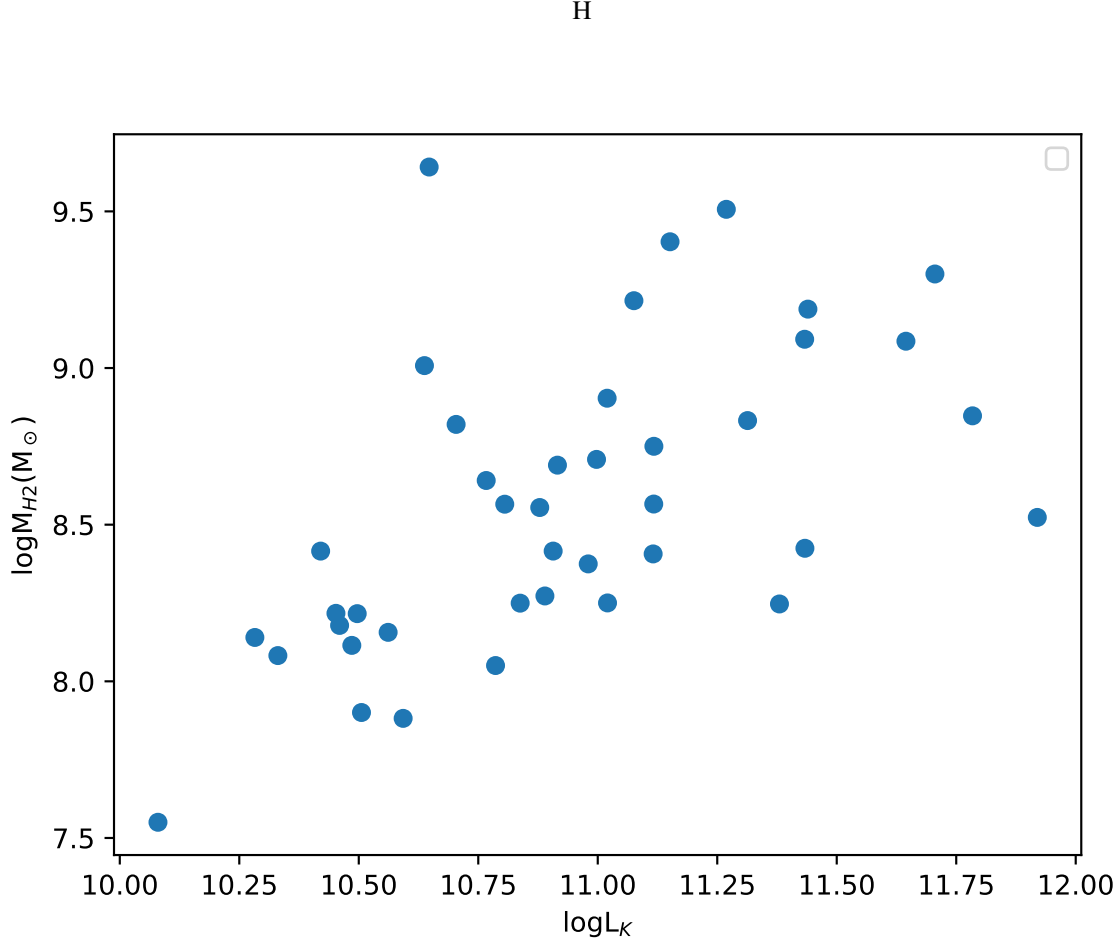


Figure 4: The K-band luminosity

## 5 Conclusions

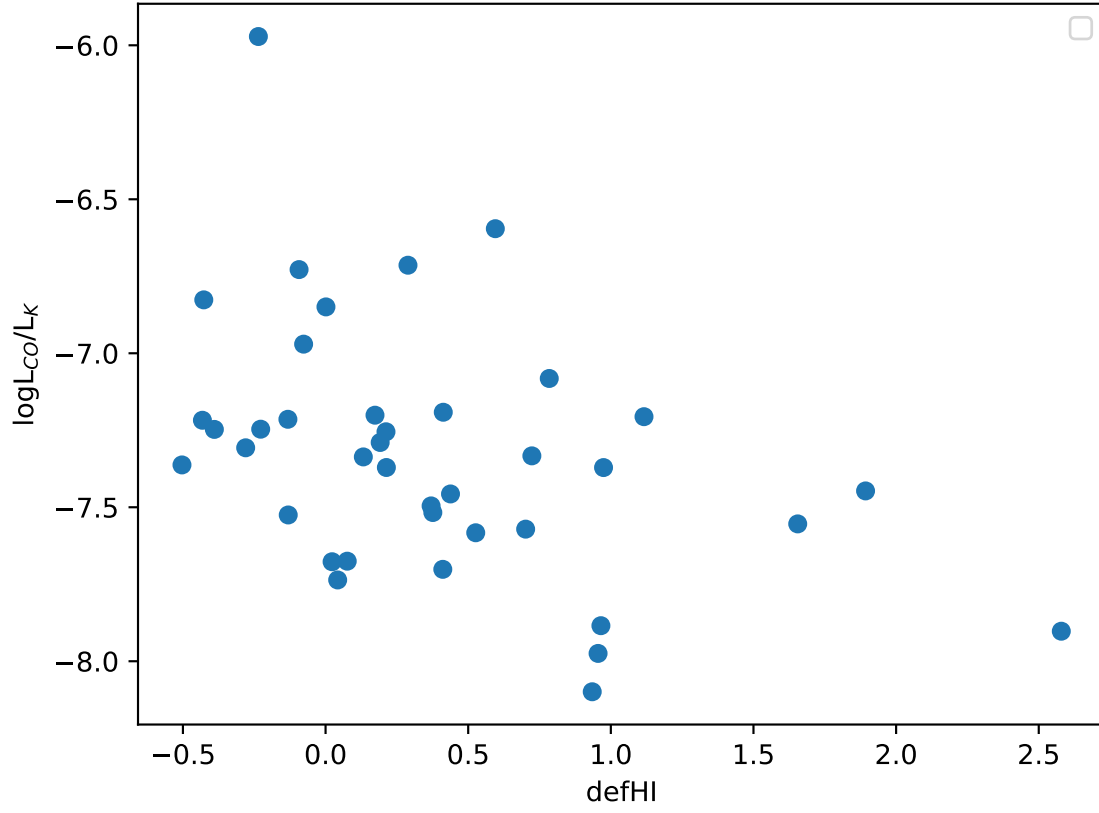
The study measured CO (J=1-0) for a sample of dusty galaxies in the Virgo cluster, selected from the Planck and Herschel surveys. The results show the molecular gas mass of 48 samples of galaxies. To study the statistical properties of molecular gas in these galaxies, combined with multi-band data (HI, optical, far infrared), to study the evolution of gas in the cluster environment and its relationship to star formation activity. The following results were obtained:

$H_2$  masses is the CO data that we observed through the 13.7m telescope at Qinghai station, by using CO-to- $H_2$  conversion factor of  $\chi = 2.8 \times 10^{20} H_2 cm^{-2} (K[T_R] km s^{-1})^{-1}$ . This is the value found by Bloemen et al(1986).in their analysis of the galactic gamma-ray emissivity.

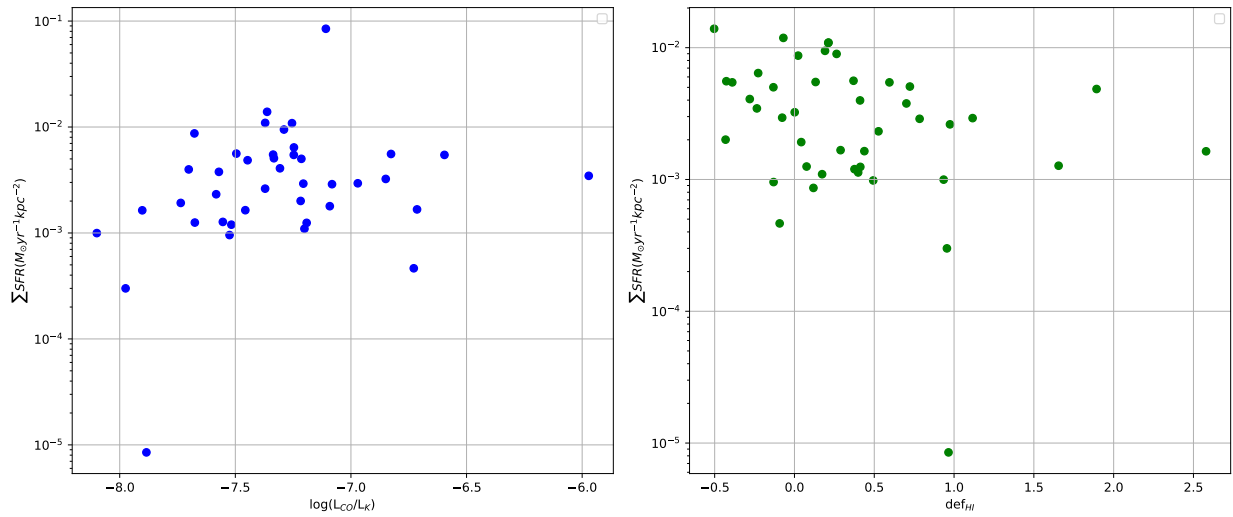
We compared the molecular gas mass with different parameters( $M_B, L_K$ )to characterize the relationships followed by galaxies in Virgo clusters. In the limited number of cases used in this study,  $M_{H_2}$  was strongly correlated with the  $L_K$  of the field sample (Figure 3), (Gavazzi et al.1996) showed the correlation of  $M_{H_2}$  with a large sample. and the  $L_{CO}/L_K$  or  $M_{H_2}/L_K$  ratio can be a reasonable amount for studying the molecular gas content of galaxies in different environments, independent of the size effect. But the correlation between gas molecular mass and B-band optical size and luminosity is weak.

According to the data collected from irsa, planck and herschel, sed fitting of galaxies is performed to obtain the SFR of galaxies. The corresponding gas dissipation time is derived from the gas mass and compared with the defHI ratio, The dissipation time of molecular gas increases with the HI deficiency, and star formation is less efficient in HI-deficient galaxies. This may be because HI is a precursor to molecular gas ( $H_2$ ), and the lack of HI limits the formation of molecular gas, thus affecting the rate of star formation.

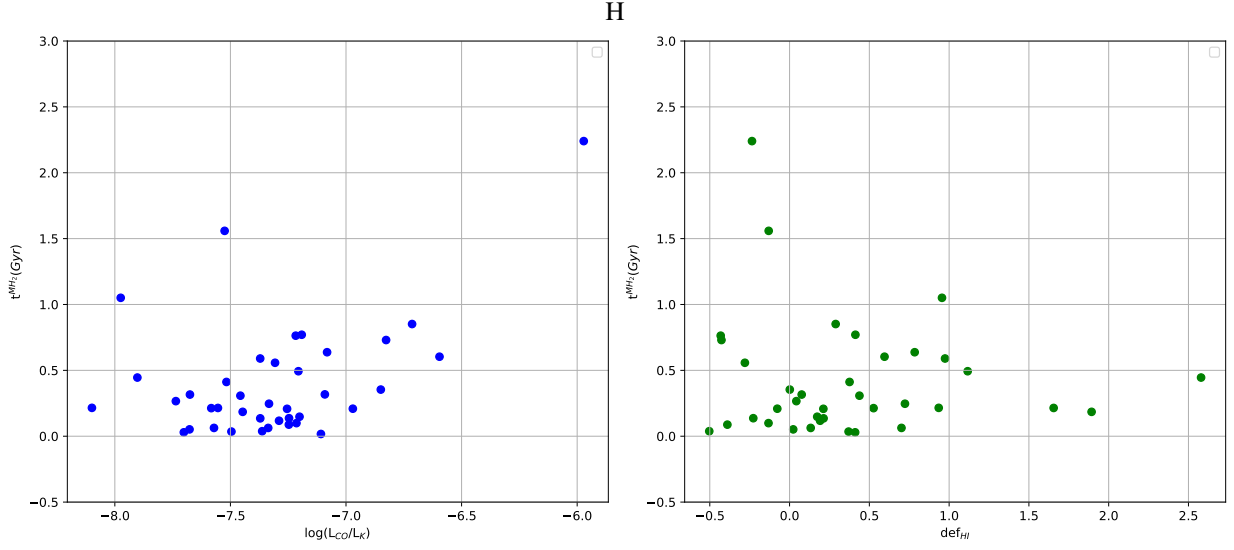
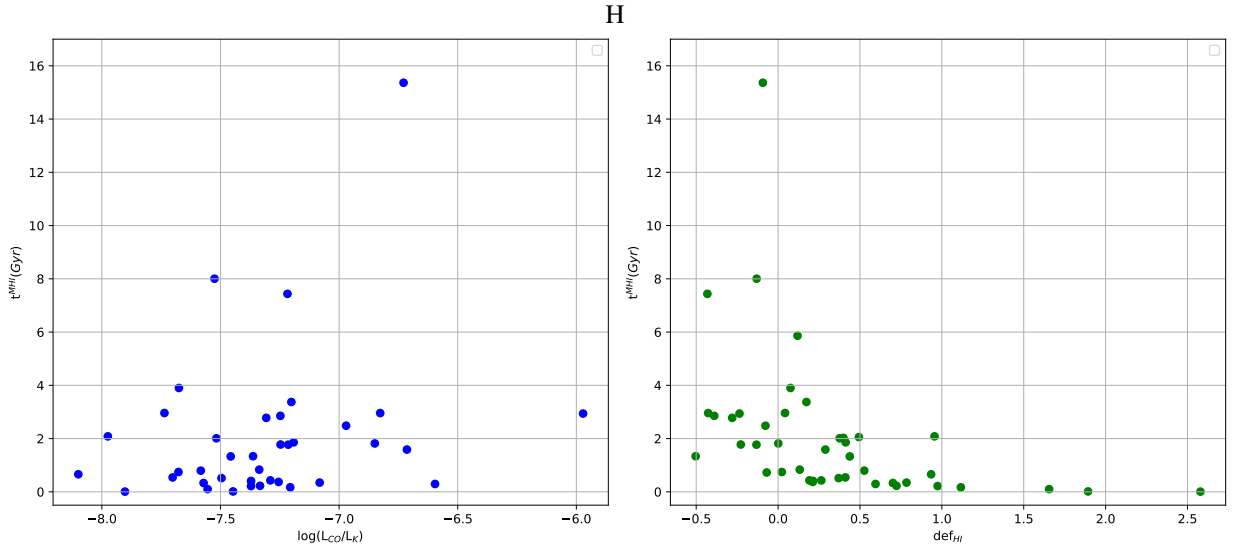
H

Figure 5: co luminosity normalized with K-band luminosity and  $def_{HI}$ 

H

Figure 6: Galactic disk mean SFR ( $\sum SFR$ ) compared to normalized CO luminosity (left) and H I defect (right).



Figure 7: Gas consumption times for the  $H_2$  gas mass  $t_{H_2}$  and  $def_{HI}$ Figure 8: Gas consumption times for the H I gas mass  $t_{HI}$  and  $def_{HI}$

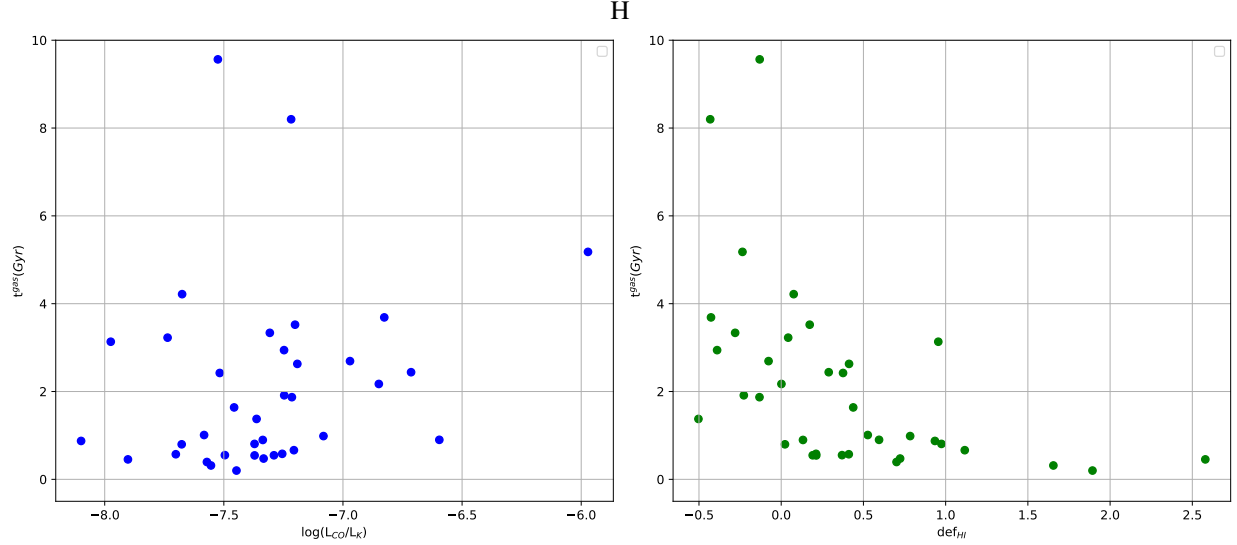


Figure 9: Gas consumption times for the total gas mass  $t_{gas}$  and  $def_{HI}$

By comparing the functional relationship between SFR and  $def_{HI}$ , it is found that galaxies with high star formation rate mostly exist in the cluster of galaxies with normal/abundant HI, which is consistent with our expectation. For SFR and  $L_{CO}/L_K$ , the SFR decreases with the decrease of  $L_{CO}/L_K$ , indicating that galaxies with lower co content have smaller SFR. This also proves that the amount of molecular gas can affect the speed of SFR. The analysis of gas consumption time in this study shows that the internal processes of galaxies in Virgo clusters are more important in the sf process than the external, ICM-driven processes.

## 6 Conclusions

The study measured CO (J=1-0) for a sample of dusty galaxies in the Virgo cluster, selected from the Planck and Herschel surveys. The results show the molecular gas mass of 48 samples of galaxies. To study the statistical properties of molecular gas in these galaxies, combined with multi-band data (HI, optical, far infrared), to study the evolution of gas in the cluster environment and its relationship to star formation activity. The following results were obtained:

$H_2$  masses is the CO data that we observed through the 13.7m telescope at Qinghai station, by using CO-to- $H_2$  conversion factor of  $\chi = 2.8 \times 10^{20} H_2 cm^{-2} (K[T_R] km s^{-1})^{-1}$ . This is the value found by Bloemen et al(1986).in their analysis of the galactic gamma-ray emissivity.

We compared the molecular gas mass with different parameters( $M_B, L_K$ )to characterize the relationships followed by galaxies in Virgo clusters. In the limited number of cases used in this study,  $M_{H_2}$  was strongly correlated with the  $L_K$  of the field sample (Figure 3), (Gavazzi et al.1996) showed the correlation of  $M_{H_2}$  with a large sample. and the  $L_{CO}/L_K$  or  $M_{H_2}/L_K$  ratio can be a reasonable amount for studying the molecular gas content of galaxies in different environments, independent of the size effect. But the correlation between gas molecular mass and B-band optical size and luminosity is weak.

According to the data collected from irsa, planck and herschel, sed fitting of galaxies is performed to obtain the SFR of galaxies. The corresponding gas dissipation time is derived from the gas mass and compared with the  $def_{HI}$  ratio. The dissipation time of molecular gas increases with the HI deficiency, and star formation is less efficient in HI-deficient galaxies. This may be because HI is a precursor to molecular gas ( $H_2$ ), and the lack of HI limits the formation of molecular gas, thus affecting the rate of star formation.

By comparing the functional relationship between SFR and  $def_{HI}$ , it is found that galaxies with high star formation rate mostly exist in the cluster of galaxies with normal/abundant HI, which is consistent with our expectation. For SFR and  $L_{CO}/L_K$ , the SFR decreases with the decrease of  $L_{CO}/L_K$ , indicating that galaxies with lower co content have smaller SFR. This also proves that the amount of molecular gas can affect the speed of SFR. The analysis of gas consumption time in this study shows that the internal processes of galaxies in Virgo clusters are more important in the sf process than the external, ICM-driven processes.

## References

- Angus Mok, C. D. Wilson & J. Golding MNRAS, 456, 4384
- Bloemen, J. B. G. M., et al. 1986, Astr. Ap., 154,25.
- Boquien, M. et al. 2019, A&A, 622, 103
- Boselli, A., & Roehlly, Y., et al. 2016, A&A, 596,A11
- Boselli, A., Gavazzi, G., Lequeux, J., et al. 1997, A&A, 327, 522
- Braine, J., & Combes, F. 1993,A&A, 269, 7
- Brian R. Kent & Riccardo Giovanelli et al. 2008 ApJ, 136, 713
- Brosch, N., Formigini, L., Almoznino, E., et al. 1997, ApJs, 111, 143
- Burgarella, D. ; Buat, V. ; Iglesias-Páramo, J. 2005, MNRAS, 365, 1413
- Combes, F., Prugniel, P., Rampazzo, R., & Sulentic, J. W. 1994, A&A, 281, 725
- Chung, A., van Gorkom, J. H., Kenney, J. D. P., Crowl, H., & Vollmer, B. 2009a, AJ, 138, 1741
- Aeree Chung, J.H.van Gorkom, Jeffrey D.P.Kenney, Hugh Crowl & Bernd Vollmer, 2009 ApJ,138,1741
- Eun Jung Chung, Min S. Yun & Marc A. W. Verheijen & Aeree Chung, 2017,ApJ,843,50
- Côté, P., Blakeslee, J. P., Ferrarese, L., et al. 2004, ApJs, 153, 223
- Casasola, V., Bettoni, D., & Galletta, G. 2004, A&A, 422, 941
- De Vaucouleurs, Gérard, De Vaucouleurs-Piétra, Antoinette, Corwin, Harold G. Jr., 1976, University of Texas press, 396, 29
- Giovanelli, R., & Haynes, M. P. 1983, AJ, 88, 881 (GH83).
- Haynes, M. P., & Giovanelli, R. 1984, AJ, 89, 758 (HG84).
- Jarrett, T. H., 2000, PASP, 112,1008
- Jarrett, T. H., Chester, T., Cutri, R., Schneider, S. E., & Huchra, J. P. 2003, AJ,125, 525
- Hewitt, J. N., Haynes, M. P., & Giovanelli, R. 1983, AJ, 88, 272
- Hibbard, J. E., van Gorkom, J. H., Rupen, M. P., & Schiminovich, D. 2001, in ASP Conf. Ser. 240, Gas and Galaxy Evolution, ed.J. E. Hibbard, J. H. van Gorkom, & M. P. Rupen (San Francisco, CA: ASP), 657
- Kenney, J. D. P., & Young, J. S. 1989, ApJ, 344, 171
- Kenney, J. D., Wong, I., Kenney, Z., et al. 2012, A&AS, 219, 246
- Kennicutt, R. C. 1998, ARA&A, 36, 189
- Kennicutt, R. C. 1989, ApJ, 344, 685
- Koopmann, R. A., Kenney, J. D. P.,& Young, J. 2001, ApJs, 135, 125
- Lisenfeld, U., Espada, D., Verdes-Montenegro, L., et al. 2011, A&A, 534, 102
- Skrutskie, M. F., & Cutri, R. M., et al.2006, AJ, 131, 1163
- Noll, S. et al. 2009, A&A, 507, 1793
- Pety, J. 2005, in SF2A-2005: Semaine de l’Astrophysique Francaise, ed.F. Casoli, T. Contini, J. M. Hameury, & L. Pagani, 721
- Planck Collaboration. 2014, A&A, 571, A28
- Edvige Corbelli1 & Simone Bianchi et al. A&A, 542, A32
- Riccardo Giovanelli, & Martha P. Haynes, et al. 2007, ApJ, 133, 2569
- Saintonge, A. 2007, AJ, 133, 2087
- Suk Kim & Soo-Chang Rey. et al. 2014, ApJs, 215, 22.
- Voyer, E. N., Boselli, A., Boissier, S., et al. 2014, A&A, 569, 124
- Wheelock, S. & Gautier III, T. N. et al. 2019,
- Young, J. S., & Scoville, N. Z. 1991, ARA&A, 29, 581
- Min S. Yun, Naveen A. Reddy & J. J. Condon ApJ, 554, 803